EXPLORATIONS OF MORPHOLOGICAL CHANGE

AT CAPE HENLOPEN, DE USING REMOTE SENSING,

RAPID-RESPONSE GPS-EQUIPPED VEHICLES AND

NUMERICAL MODELING

BY

CHRISTINA A. LINDEMER AND JACK A. PULEO

CENTER FOR APPLIED COASTAL RESEARCH

Ocean Engineering Laboratory
University of Delaware
Newark, Delaware 19716

ACKNOWLEDGMENTS

TABLE OF CONTENTS

LIST OF TABLES

v

LIST OF FIGURES

ABSTRACT

Delaware beaches are influenced by north-directed sediment transport for the majority of their length, starting at a fluctuating sediment transport nodal point, near Bethany Beach. Northerly transport terminates at the Cape Henlopen Spit, a morphological feature located at the northern tip of the coastline. Over the past 250 years, this littoral sink has matured from a cuspate headland growing 2 km into a simple spit, fed by the eroding Delaware coastline. Despite rapid development, few studies have been completed on the nature and causes of this remarkable expansion. This exploration provides methods to produce comprehensive datasets for quantifying the short term morphological development at the Cape, along with the hydrodynamic conditions governing the region. A video-imaging system was installed at the Cape to supply shoreline position, planform information and insight into the alongshore variability in breaker intensity. Several rapid response GPS-equipped vehicles were developed to acquire robust survey data covering the Cape's offshore bathymetry, intertidal zone, beach face and dune fields. Current meters and pressure sensors were deployed for several tidal cycles, on a small intertidal bathymetric feature on the bayside and a stretch of the oceanside of the Cape to study the currents in the region. Finally, a numerical model was tested to examine its ability to simulate morphological change due to large weather events, in order to determine its appropriateness for use along the Delaware coastline.

Chapter 1

INTRODUCTION

1.1   Overview

The east coast of the Delmarva peninsula is made up of a barrier island-lagoon morphology, with the mouth of the Chesapeake bay as the southern terminus, and the mouth of the Delaware bay as the northern terminus (Figure 1.1). Near Bethany Beach, Delaware there exists a fluctuating sediment transport nodal point, where the yearly average net transport diverges. Sediment moving north from this nodal point encounters two major features of the Delaware coastline, the Indian River Inlet, and Cape Henlopen spit complex. The Indian River inlet alters the natural rate of sediment transport along the coast, while transport mostly terminates at the Cape Henlopen spit. There is some transport onto Hen and Chicken Shoal, offshore of the spit, but it is outside of the realm of this study.

The Indian River Inlet is a hard structure inlet, constructed by the US Army Corps of Engineers (USACE) in 1939. The inlet quickly showed the typical side effects associate with hard structures, highlighting the northerly sediment transport along this section of the coast. The down drift, northern side of the inlet quickly eroded, as the southern side grew wider. In 1990, a sand bypassing system was installed by the USACE in order to protect the down drift beach, and the US highway that was in danger of being overwashed. This bypassing system attempts to mimic the natural northerly littoral transport at the site, and throughout the first few years of existence, averaged 76,456 m^3 /

year bypassed (USACE, 1994). The bypassed quantities have an average rate now that is much lower. New studies based on modeled wave data and the Coastal Engineering Research Council (CERC) equation for alongshore transport found northerly transport at $-373,191$ m^3 / year with a standard deviation of196,201 m^3 / year (Puleo, 2010). This bypassing system originally had the intention to mimic sediment transport along the Delaware coastline, however the rates seem to be falling short.

North of the Indian River Inlet, the next major feature affecting sediment transport is the terminus point for the Delaware coastline, the Cape Henlopen spit complex (the Cape). This spit is located at the mouth of the Delaware Bay, near Breakwater Harbor. Maps from the 17th - 19th century show Cape Henlopen as a broadly rounded cuspate-type spit that in the past 250 years has grown on the order of 2 km into a simple spit formation (Maurmeyer, 1974). Such extensive growth is due to gradients in the sediment transport along this coastline. However, these gradients have not been extensively studied, nor the importance of the tidal and wave processes governing this growth. Recent estimates for this area, based off of modeled wave data and the assumed CERC equation for alongshore transport and shoreline alignment, have been on the order of 517,088 cu m^3 / yr with a standard deviation of 241,313 m^3 / year (Puleo, 2010).
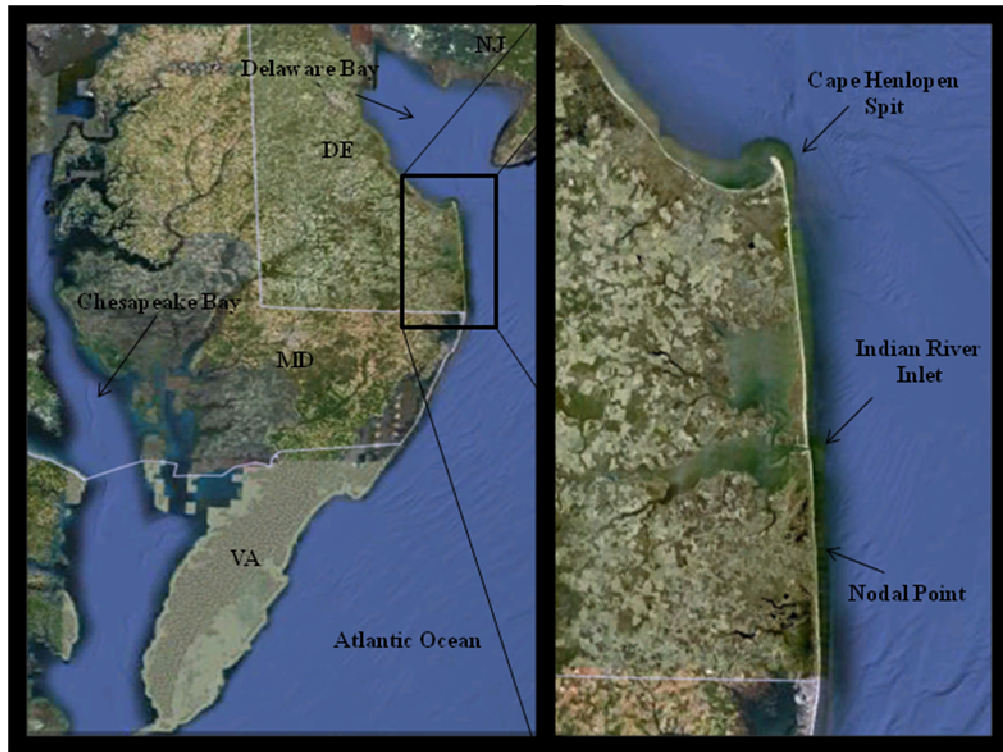
Figure 1.1: The Delmarva Peninsula (left) and the Delaware coastline (right) (Google Earth, 2010). State abbreviations and names of bodies of water have been superimposed on the image, along with points of interest.

This study presents a preliminary investigation into the morphological change at the Cape, discusses procedures for further exploration. In order to accomplish this, several methods are explored. A video imaging system was used to acquire shoreline and planform information in the region, while also providing alongshore variability in wave direction and intensity on the ocean side (Chapter 2). Rapid response vehicles equipped with GPS are used to collect bathymetry and sub-aerial topography, including: a jetski with sonar, a dolly for foot surveys and an all-terrainvehicle for beach face surveys (Chapter 3). Tripods equipped with current meters, and pressure sensors were deployed on a small morphologic feature on the tidal flats on the bayside of the Cape, along the oceanic side of the Cape, in order to evaluate their ability to identify deviations in current strengths between different sensors (Chapter 4). Lastly, a recently developed numerical model was explored in order to determine its appropriateness for future studies at the Cape (Chapter 5). Future work will be discussed in Chapter 6.

1.2   History of Cape Henlopen

The Cape Henlopen Region, first home to a local tribe of Lenni Lenape Indians, was first discovered by Westerners in 1609 by Henry Hudson as the land where the Atlantic Ocean and Delaware Bay met. The region was quickly settled with a port, by the Dutch and Swedes, becoming the first settlement in Delaware. In 1767, the Cape Henlopen Lighthouse was placed on the shores of Cape Henlopen to help guide vessels into the Delaware Bay, however it was destined to fall in to the ocean 159 years later due to significant beach erosion. An inner breakwater was constructed between 1829 - 1931 and an outer breakwater was constructed in 1890 (Maurmeyer, 1974) (Figure 1.2). Due to the

4

early settlement on the Cape, heavy utilization as a port town, and being the site of major engineering projects, maps of the region date back to the 1700's.

These maps make it very clear Cape Henlopen spit is experiencing rapid growth. Much of this growth can be attributed to the sediment supply from eroding headlands along the Delaware coastline. The erosion of the coast, and subsequent growth of the spit is made clear when the old Cape Henlopen Lighthouse is used as a reference. When the lighthouse was first installed, in 1767, it was roughly 490 m from the Atlantic Coast, and was 1005 m from the northern tip of the Cape. It fell into the Atlantic Ocean during a spring storm 1926. At this time the growth of the Cape was noticeable (Figure 1.2), compared to earlier maps of the Cape (Figure 1.3). The eroding beach to the east of the lighthouse undoubtedly contributed to the development of the Cape during this period due to prevailing northerly direction of sediment transport in this region.

Between the installation of the lighthouse, and a map by William Strickland, created in 1831, the spit advanced 335 m at a rate of 5 m per year. Coastal erosion was estimated to be 1 m / year in this area during the same period. By 1933, the tip of the Cape was 2380 m from the former location of the lighthouse, a growth of 1370 m (Maurmeyer, 1974). Based on a combination of air photos by J.C. Kraft in 1968 and an unpublished survey by Miller, Wakefield and Maurer in 1972, Maurmeyer (1974) estimates the rate of accretion has increased to over 18 m per year. The tip of the Cape is 3.2 km from the location of the former lighthouse.

Beach nourishment projects began on the oceanic Delaware coastline in 1988 (Chrysalis, 2007) and have continued to present day, occurring every few years in different beach towns. These nourishment projects, often placing hundreds of thousands of

5

cubic meters of sand on the beach at a time, provide the material that the littoral cell cycle in Delaware demands. North of the nodal point (Figure 1.1) in Bethany Beach, the sediment from the nourishment projects continues to travel north along the Delaware beaches until it reaches the Cape Henlopen spit. This nourishment has allowed a relative stabilization of the Atlantic coastline, however the Cape Henlopen spit continues to grow.

In the past, there have been a few studies of this site, with most focusing on Lewes Harbor, and the associated infilling from sediment off the tip of the point including: Kraft and Caulk (1972), Maurmeyer (1974), Demarest (1978), Demarest and Kraft (1979), Hoyt (1982) and Pratt (2007). A few have touched on the growth of the spit, and the associated sediment transport gradients (Kraft and Caulk, 1972), (Maurmeyer,1974) however the spit has not been extensively studied in decades, well before the beginning of nourishment projects on the Delaware coastline, resulting in a need for this study.
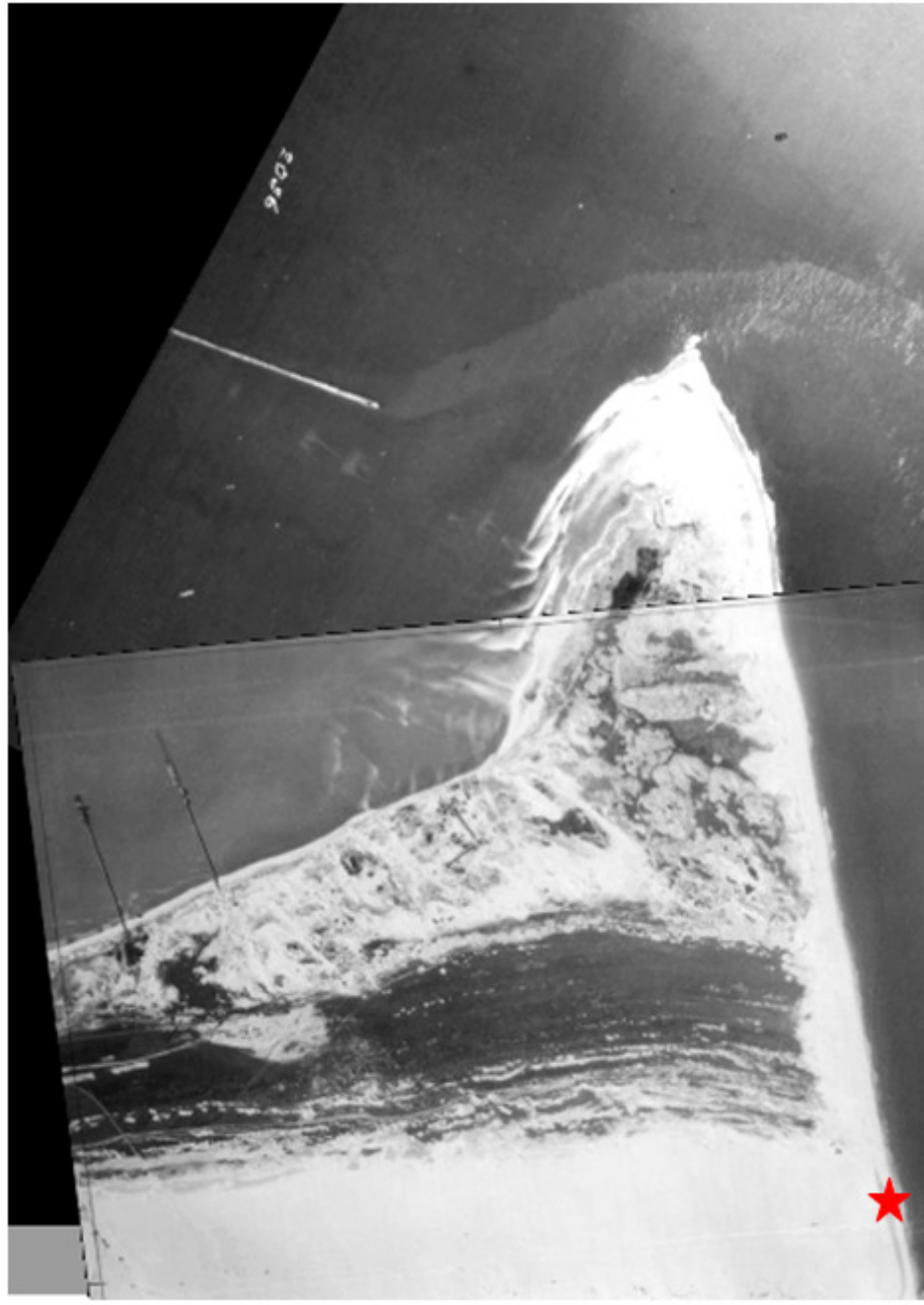
Figure 1.2: Cape Henlopen Spit, 1926. The location of the lighthouse is noted with a red star. (Ramsey, 2001)
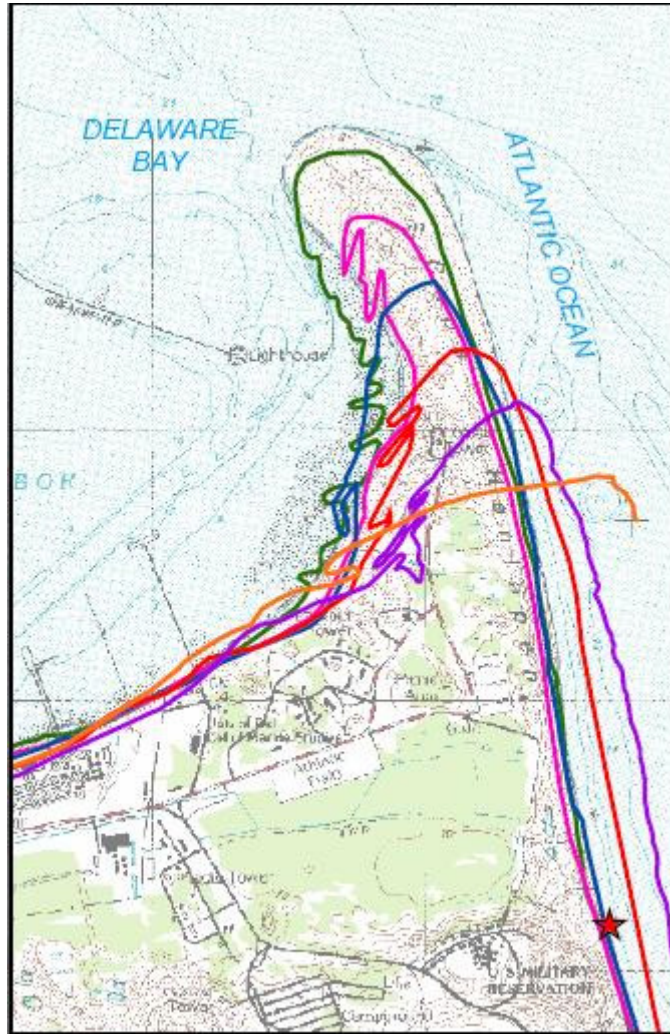
Figure 1.3: Map showing the growth of the Cape relative to the Lighthouse (red star). The lines represent the following shorelines: 1842 (orange), 1884 (fushia), 1918 (red), 1944 (blue), 1954 (pink), and 1977 (green). (Ramsey, 2001)

Chapter 2

VIDEO-IMAGING SYSTEM

2.1   Overview

The installation of a video-imaging system near Cape Henlopen Point (Figure 2.1) provides valuable information on the shoreline position, planform information and insight into the alongshore variability in wave direction and intensity on the ocean side. Video imaging systems have been successfully used in the past to achieve such goals (Lindemer, 2008

; Pearre et al., 2009; Turner et al., 2006).

Video imaging systems are used to create a high temporal resolution data set of a remote beach location. Rob Holman, of Oregon State University, developed a video-based system, Argus, to observe the coastal environment (Holman, 2007). This video-system, used as a model for the Cape Henlopen site, provides a dense and accurate sampling of the coastline's position, that is needed when dealing with a stretch of coastline as large as the Cape. Similar methods have been utilized with high success rates in computer vision and robotics to measure physical quantities. This method has received high acceptance rates (Holland et al., 1997). The technique employs a set of calibrated video cameras on a remote, static and elevated position, where the images are recorded and stored on a host computer. Once collected, both quantitative and qualitative information are extracted from the image to provide insight into shoreline location and wave parameters. The user defined sampling

frequency is usually on the order of an hour for the purpose of quantifying shoreline position, and provides data sets that can span for several years, providing a time range of observable processes from tidal to accretion/erosion due to seasonal variations.

Using the Argus system as a model, the methods to configure, calibrate and quantify information collected by the system are based on well known camera optics (Holland et al., 1997). The calibration process identifies the variables associated with the system, including the intrinsic parameters of the camera lens, and image acquisition software, along with the physical parameters of the real world location of the cameras, allowing a transformation between oblique pixel location *(U,V)* to *(x, y, z)* real-world locations in the image. This transformation provides a planform, or 'bird's eye view' of the area of interest (AOI).

The University of Delaware's Surf and Nearshore Dynamics Camera (SANDCam), is a monitoring system that utilizes the basic methods and structures of Argus, current methods employed by SANDCam and user defined algorithms for isolating shoreline in the AOI. Sites have been successfully placed in Rehoboth Beach and Bethany Beach, Delaware and Cape May, New Jersey.

2.2   Set-up

Once the necessity of a video-imaging system on the Cape was determined, the location was selected (Figure 2.1), providing a clear, static, and elevated position near the AOI away from interference from human and natural factors. Once receiving permission from DNREC, an 18 m tower was constructed where 8 cameras were to be placed on top (Figure 2.1) providing a view from the bay-side to the ocean-side of the Cape.

With knowledge of the *(x, y, z)* location of the cameras wi

th proximity to the shoreline and height above sea level, resolution mapping was completed

to determine the ideal configuration of lenses in order to provide a wide range of view with

high resolution in the shoreline region. This resolution mapping provides information on the

principle configuration of the camera lens focal lengths and the preliminary azimuthal angles

for the camera configuration. The associated variables with the resolution mapping are: the

horizontal fields of view *(FOV)* for several different focal lengths given the cameras charge-

coupled-device *(CCD)* size, and the azimuth (horizontal) and tilt (vertical) angles in relation to

the horizontal and vertical axis of the set-up. Using methods from Holland et al. (1997) each

pixel can be mapped onto a ground plane using image projection procedures.

The resulting image is a color map (Figure 2.2) corresponding to the cross-shore

and alongshore pixel footprint as a function of cross-shore and alongshore distance. Blue in

the color map indicates a pixel footprint representative of one meter in the cross-shore (or

North-South) direction. Red indicates a pixel footprint of   10 meters in the cross-

shore direction. It is ideal to have the smallest pixel footprint possible to ensure image

clarity and accurate shoreline analysis. The resolution map for Cape Henlopen indicates a

representative resolution of <5 m for the entire cape.

This resolution map is based on a camera lens configuration as follows (from

East to West or counter-clockwise): 6 mm, 9 mm, 12 mm, 12 mm, 12 mm, 50 mm, 50 mm,

25 mm and 6 mm, with each lens overlapping. A 50 mm lens has a smaller field of view (~7

˚) but a higher cross-shore resolution a distance away from the camera vs. a 6 mm lens with

a larger field of view (~55˚) but a lower cross-shore resolution a distance away from the

camera. These intrinsic characteristics of camera

Figure 2.1: Location of the tower that holds the video-imaging system, comprising of 8 cameras.
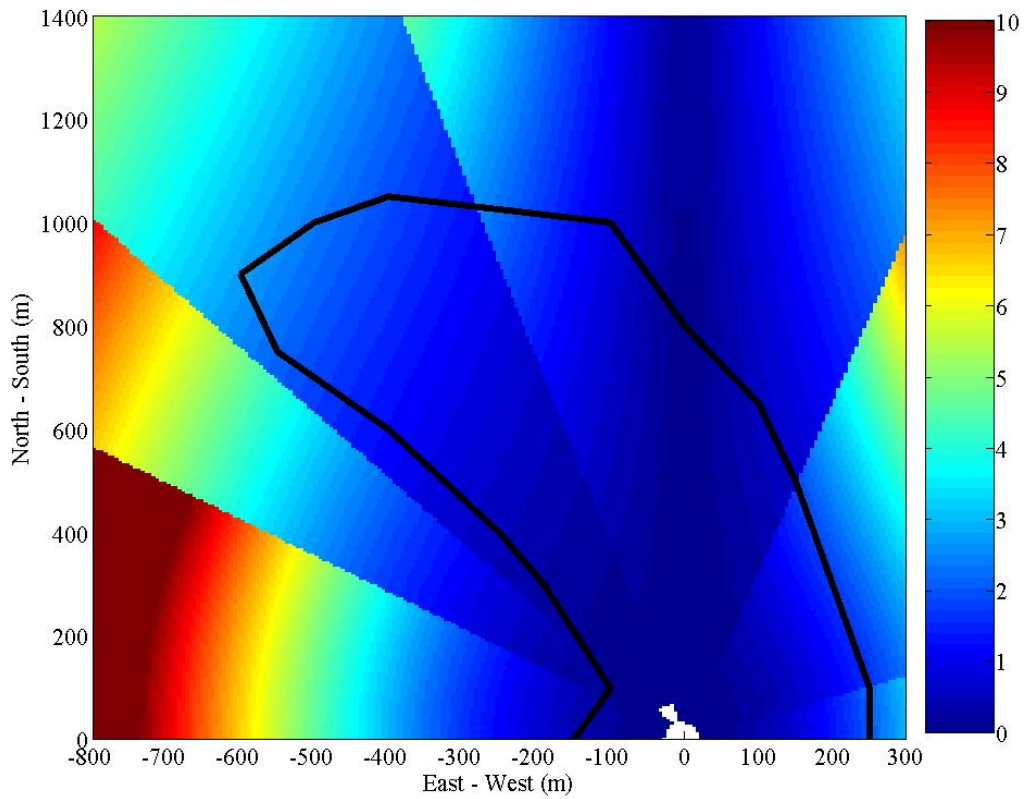
Figure 2.2: The cross-shore resolution of the cameras at Cape Henlopen. The camera's location is at (0, 0) on the map, with the North-South/East-West distances indicated on the axis. An outline of the Cape has been superimposed on to the image, in order to show the pixel-footprint at a standard shoreline. The colorbar indicates the size of the cross-shore pixel footprint (m).

lenses, led us to have the 50 mm lenses focused at the tip of the Cape that is nearly 1 km from the camera locations, and the 6 mm lenses focused on the near bay- and ocean-side shores that are anywhere from 100-250 m away from the camera site.

The selected lenses have unique and inherent distortion associated with them due to lens curvature and glass imperfections. These distortion parameters must be solved for before the cameras are installed on the site. They are regarded as the intrinsic parameters of the lens and camera, and do not change based on camera location or orientation. They are determined in the lab following the procedure described by Holland et al. (1997) where the distortion is modeled as a cubic function of radial distance from the center of the lens.

Maintaining a controlled environment throughout the entirety of the image collection is crucial while solving for the distortion parameters. An image of (15x20) white dots on a black background (Figure 2.3) is place on a flat surface that is parallel to the camera's focal plane. When properly positioned, the camera will have the focal plane of the lens parallel to the image, the collected image filling the field of view and no inadvertent azimuth, tilt or roll angles associated with the orientation. During data collection in the lab, the image collected was ensured to be parallel with the plane with the use of right-edge rulers and the image collection software's built in horizontal and vertical line features. Divergences from the ideal set-up will become apparent visually due to the radial nature of the distortion and the standard deviations of the parameters themselves.

Each lens is used to collect three images, and the image with the least pixel error upon solution of the distortion parameters is employed. With decreased focal length (

50 mm - 6 mm) the distortion becomes more perceptible (Figure 2.4). The center of the

white dots are identified using center of mass calculations, along with the center of the

image (Figure 2.5) . This apparent distortion is compared to the predicted, undistorted,

position of the dots without distortion (Figure 2.6). After this analysis is complete, the

intrinsic parameters are identified (l_v, l_v, U_0, V_0, D_{ist1}, D_{ist2}). l_x and l_v are the vertical and

horizontal scale factors related to pixel squareness, with u_0 and v_0 are the image center

relative to a 640 x 480 image (note: the image collected is 1280 x 1024), with D_{ist1} and D_{ist2}

as the lens distortion coefficients employed to establish the error as a function of radial

distance, *r* (Holland et al., 1997).

$$\Delta r = D_{ist1}r^3 + D_{ist2}r, \quad (1)$$

Once the location, resolution and intrinsic parameters are determined, the site

can be set up. As mentioned, the cameras were placed atop a 18 m tower (Figure 2.1). The

cameras used are color uEye (model UI-1540-C) USB 2.0 with a ½" CCD (Figure 2.7). They are

high powered ultra compact cameras. The camera lenses had a polarizing lens attached to

the outside to reduce glare. These cameras were housed in white Pelco housings (as seen in

Figure 2.7) with desiccant placed inside each housing to reduce moisture buildup.

Two computers were used to control 4 cameras each (Computer one - cameras

1-4 and Computer two - cameras 5-8). The computers collecting the images were Asus

EeePC, Windows XP based mini-laptops, equipped with camera controlling software (VM95)

by Erdman Video Systems to initiate camera collection. The VM95 software allows for user

defined flexible scheduling of image collection types and times implemented as the system

requires. They were housed inside a small building
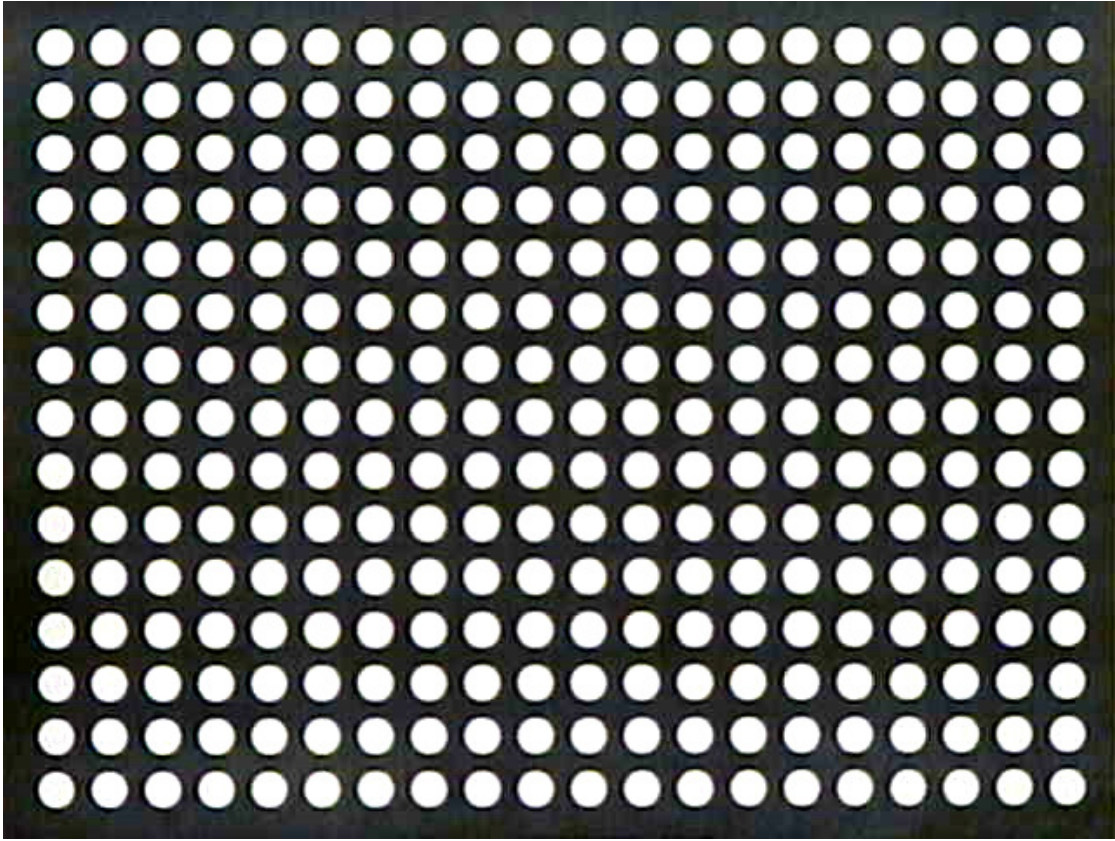
Figure 2.3: The image used in the calibration processes. Equally spaced white dots (15x20) on a black background. Deviations from this pattern are used to determine the camera lens distortion parameters.
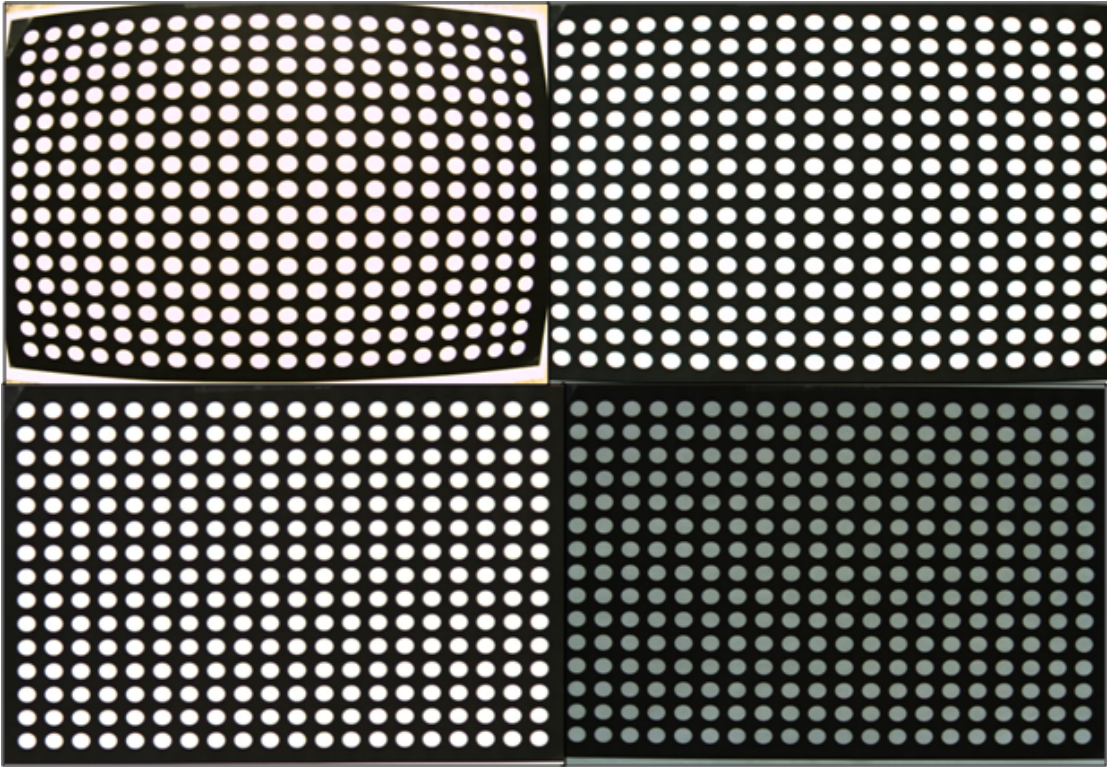
Figure 2.4:   Clockwise from top left to bottom left the distorted image for a 6 mm lens, 9 mm lens, 25 mm lens, 50 mm lens.
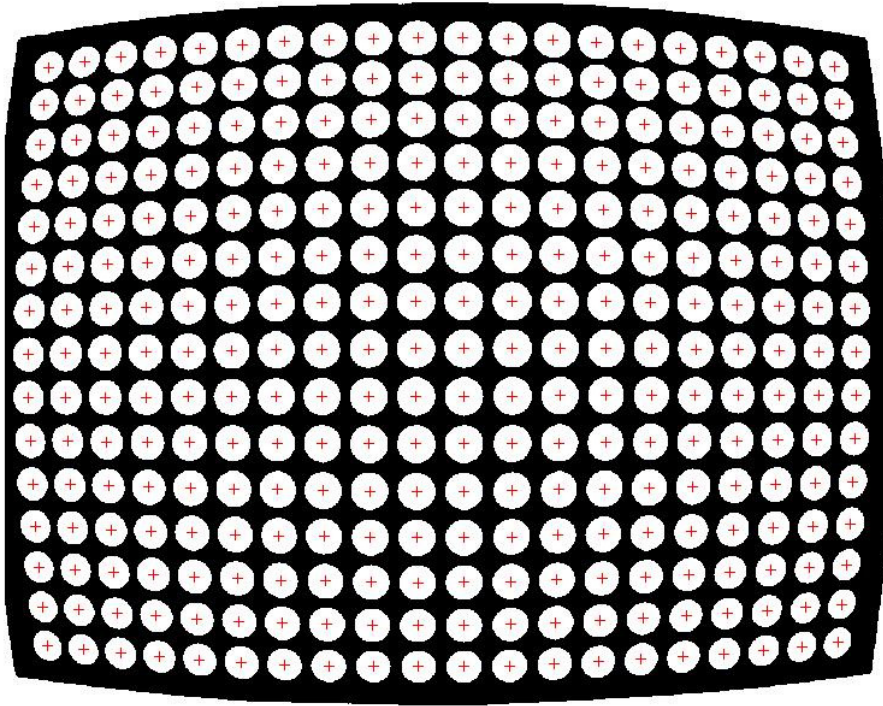
Figure 2.5: **A processed distorted image (6 mm) with the dot center identified for every dot and marked with a red cross.**

Difference

U stddev = 11.314
V stddev = 9.672
Dist1 (R^3) = -2.774e-007
Dist2 (R^3) = 0.08046
Uo = 627.0
Vo = -508.5
1/lx = 1.000

Remaining:
U stddev = 2.1517
V stddev = 3.2889

Correlation

Error after correction
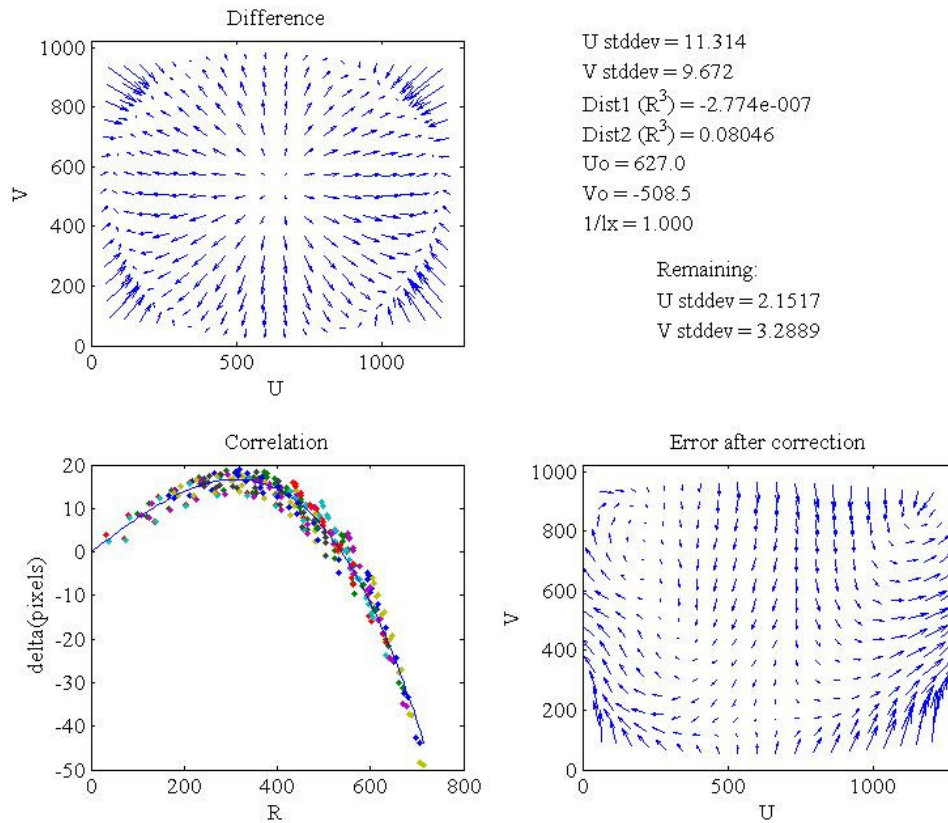
Figure 2.6:   Analysis of the processed image. The top left shows the location of the expected pixel location vs. the apparent location, with the tail of the error being the expected position and the point being actual location. The bottom left shows the pixels being fitted to the cubic function (eqn. 1), with the variable outputs in the top right.

~100 m from the tower that belongs to the River Pilot's Association. Connecting the cameras to the building were 60 m cables, protected in PVC conduit, running from the cameras, down the side of the tower and into the building, where they connected to the corresponding computer (Figure 2.8). A SWAP radio, provided by the University of Delaware, was attached to the top of the tower, and fed via the cable bundle to the computers providing internet access to both. The computers are programmed to temporarily store the images before transferring them to the University of Delaware's Center for Applied Coastal Research to be stored in the SANDCam archive system.

Each camera collects three types of images, every hour, during daylight hours. These are the snap, timex, and variance images (Figure 2.9). The snap shot (Figure 2.9 a) is collected at the beginning of the hour and gives insight into the conditions that hour, such as large waves or rain. The next image is the timex (Figure 2.9b), or time exposure image, averaging the pixel intensity of the images over ten minutes. This smoothes out the breaker zone into a white strip, making the shoreline more apparent and transient features (such as people or individual waves) become less visible. Timex images provide helpful insight into the location of features such as sandbars, rip currents and the breakpoint position.

The variance image is the third type of image collected (Figure 2.9 c), and highlights the locations where the image is experiencing high variability such as the surf zone where the pixel intensity is not relatively constant (pixel goes from dark sea water to white turbulent water). Areas where there is high variability are mapped to white, while the static portion of the image is mapped to black or dark green. This image type has been helpful to isolate breakpoint and shoreline regions in active surfzones.

Figure 2.7: The uEye camera used in the project (Lindemer, 2008).

Figure 2.8: The top of the tower with the cameras attached in their housing (top) and the tower with the building storing the computers in the foreground.

The cameras were installed in November, 2009. While the tower was being installed, Ground Control Points *(GCPs)* were placed on the beach. Each field of view needs five GCPs, with two in the overlap between neighboring cameras. The necessity for these GCPs will be discussed in the next section. Once the tower was intact, and the cameras placed on top, all wires were connected and images were collected showing the GCPs in the field of view (see Section 2.3).

2.3   Field Calibration and Image Rectification

In addition to the intrinsic parameters, calibrated in the laboratory, there are explicit parameters that are unique for each set-up of the imaging system, and can change with a drastic movement of a camera's position. The explicit parameters are x_c, y_c, z_c, f, σ, τ, and φ; they relate the camera position and orientation to a real world coordinate system. x_c, y_c, and z_c are the real world coordinates of each camera's location on the tower, and f represents the effective focal length of each camera's lens. σ, τ, and φ represent the roll, tilt and azimuth of the camera's set-up as depicted in Figure 2.10.

After identifying these variables, it is possible to complete the image rectification. This process relates the (u, v) pixel location seen in an oblique image to the real world (x, y, z) location of this point as shown in the rectified (x, y) plane at a specified z elevation. In completing this process, the camera positions are surveyed along with several GCPs that have been placed in each FOV.
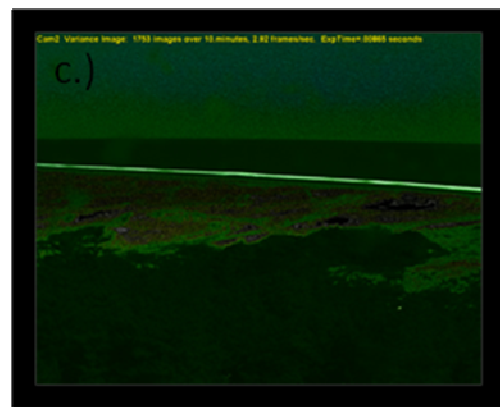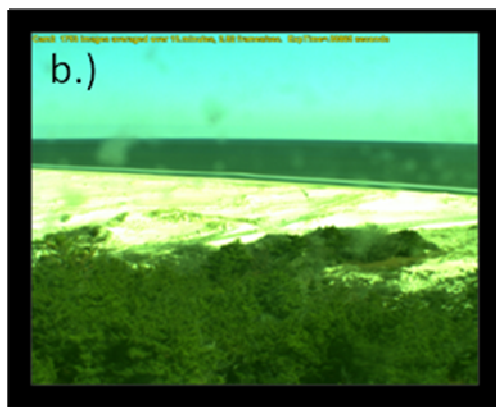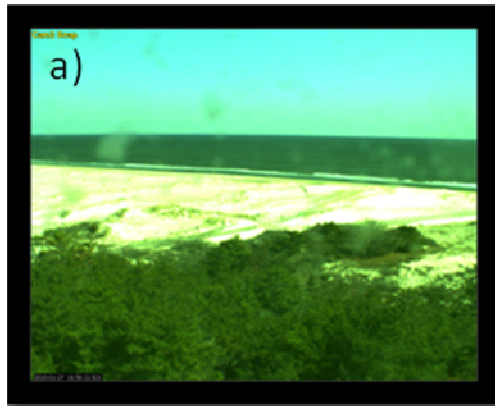
Figure 2.9: a.) Snap shot image, where individual waves can be seen. b.) Timex image, or time exposure image, where collected images are averaged over ten minutes. c.) Variance image, where high pixel intensity variance is highlighted in white and low pixel intensity variance is colored to black or dark green.

Each camera, once on the tower, is aligned to collect the desired image of the beach, with slight overlap of FOV between each camera. This is an important part of 'stitching' the images together in the rectification process. It is helpful if there are static objects in the FOV, such as buildings, poles, parking lots or (in our case) lighthouses that are then used as permanent GCPs. The permanent GCPs can be referenced long after the initial installation to detect any changes in the tilt, roll or azimuth angles, and re-rectify the images if any changes in angle occur, without re-visiting the site. In addition to the permanent GCPs, numerous temporary black GCPs ranging in sizes from 0.6 to 2.4 meters across are placed in each camera's FOV (Figure 2.11). Surveying was done using a Magellan ZMax RTK-GPS surveying system, using a real time cellular modem linked a network of base stations rather than a local base station to acquire datum information. The coordinate system used was UTM (meters).

Once the intrinsic and explicit parameters are solved for, an oblique image of the coast can be mapped to either a ground plane, or panoramic view, in a procedure known as rectification. There are two equations describing the relationship between real world coordinates (x, y, z) and image pixel location (u, v), leaving the system underdetermined (see Holland et. al., 1997), therefore the ground plane (z coordinate) must be specified in order to rectify.

For the Cape Henlopen planform view, the ground plane was chosen as the predicted tidal level for each hour of interest (using the XTIDE tidal harmonics package; www.Flaterco.com/xtide/). Rectification is performed to a specified grid in UTM coordinate system for each image, allowing for the individual images to be stitched together producing a merged ground plane view of the AOI, analogous to what would be seen from an overhead

view (Figure 2.12). Having the imagery cast into a known coordinate system allows for the feature lengths and information to be quantified.

However, in this case, the merged ground plane view (Figure 2.12), is not preferable due to dune obstruction at the shoreline and false mapping of the dunes and trees to tidal levels when their actual elevations are much higher. Instead, a panoramic view was created of the shoreline, using in-house codes (Figure 2.13). The axis numbers are in pixel size. This image gives a much less distorted view of the cape, and its extensive shoreline, while also showcasing the elevations of the dunes where GCPs were located and surveyed.

2.4   Shoreline Identification

In the past, there have been several methods used to identify the shoreline in the images supplied by a video-imaging system. Plant and Holman (1997) implemented a video imaging system at the Duck, NC Argus site, with shoreline identification taken from the gray-scale time-exposure image. The shore-break intensity maximum (the white strip in the timex image associated with the swash zone) was modeled in specified cross-shore transects with a parabolic curve. This allowed the determination of the maximum intensity, within a confidence interval gained from the width of the parabola that was then marked as the shoreline. When no discernable shoreline was available (caused by poor weather or light conditions), or the parameters found in the parabolic fit were outside set limits, no shoreline would be identified. Compared against traditional survey methods, this estimation of the shoreline was found to be 3 m shoreward of where traditional surveying would place the shoreline (std = 4.9 m). This study helped solidify video imaging as an acceptable and robust technique for shoreline identification.
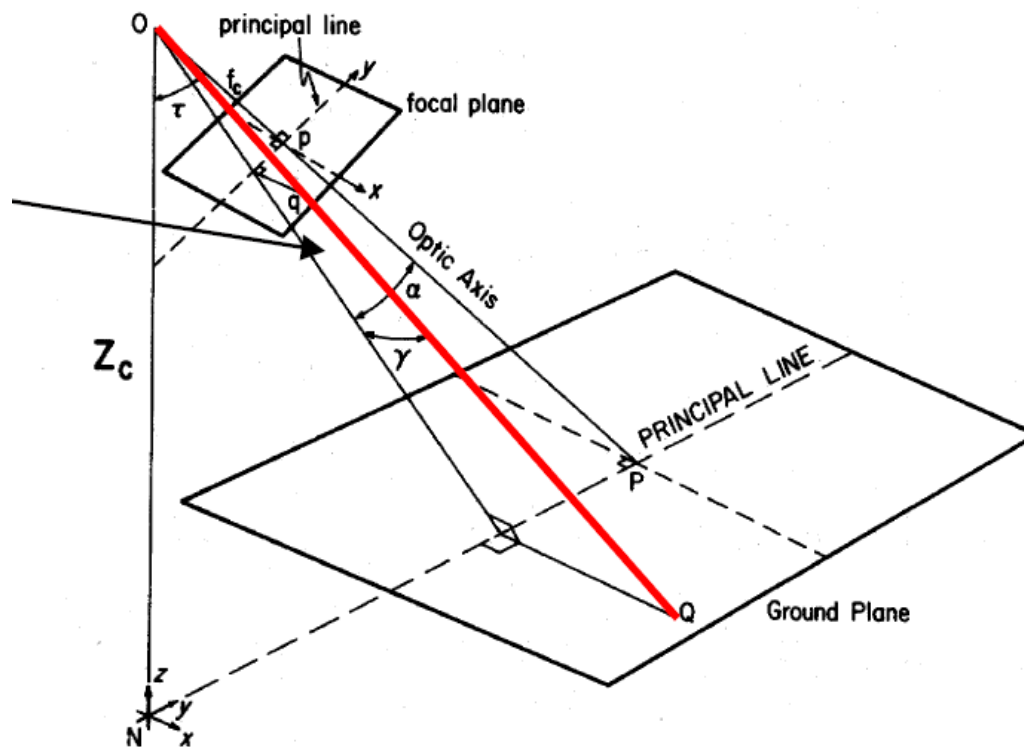
Figure 2.10: Relationship between the camera's (x_c, y_c, z_c), the image (u, v) coordinates, (x, y, z) world coordinates and the rotation angles (σ, τ, φ). (Holland et al., 1997).

Figure 2.11: Ground control points in an image are highlighted with red arrows. There are permanent (lighthouse) and temporary (black/white squares) GCPs.
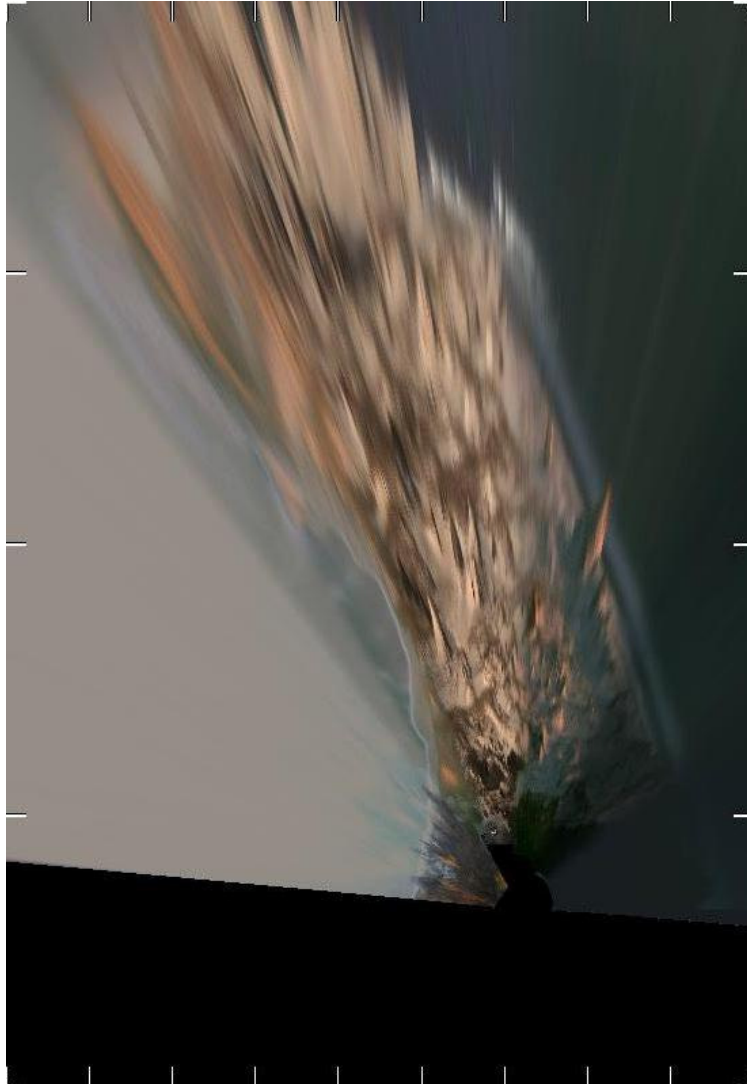
Figure 2.12: Merged image of the Cape Henlopen shoreline. The space between the white tick marks is 175 m. Trees and dunes (with much higher elevations) have been mapped to ground level causing them to obstruct the shoreline in some areas, and smear out into the water. Due to this, individual oblique images will be used to identify the shoreline, with the pixel (u, v) coordinates then being transformed into real world (x, y, z) coordinates (Section 2.4).
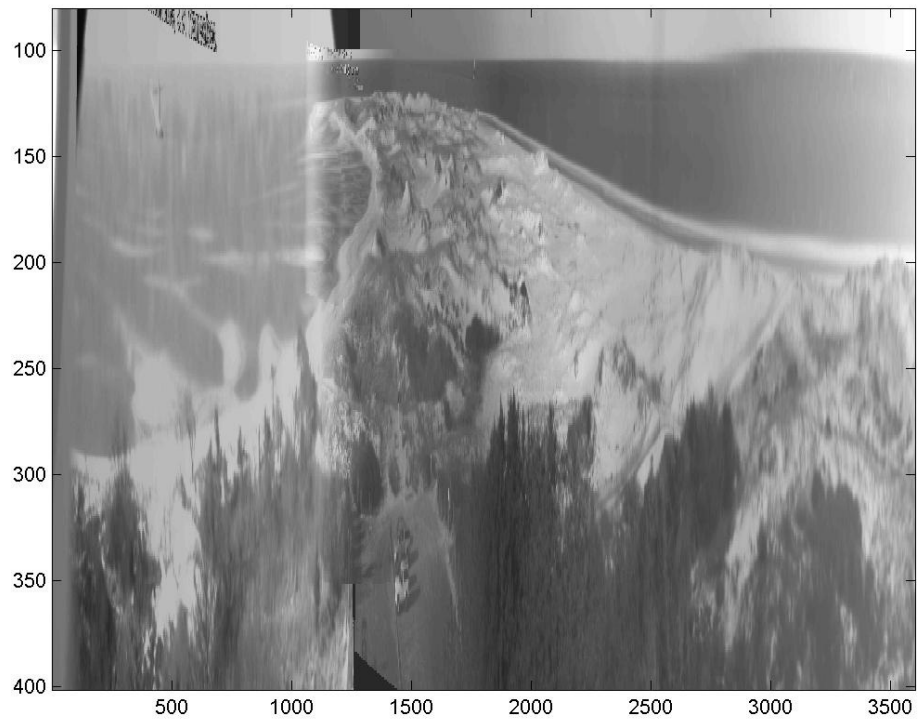
Figure 2.13: Panoramic view of the Cape looking to the North. The axes are in pixel numbers. In this image, dunes that hosted a GCP during surveying have been mapped to their correct elevation, and are not smeared across the field of view as they are in the previous figure.

Aarninkhof and Roelvink (1999) presented a model for identifying the shoreline utilizing the RGB (red, green, blue) images. The method allows for the automated video imaging system to be placed in an area where there is no discernable shore-break intensity maximum, due to gently sloping beach faces with no defined break, or where features such as inner sandbars occasionally emerge from the water at low tide. This model is seemingly more robust than the Plant Holman (1997) method, since it can be used in a wide array of beach types.

In the Aarninkhof and Roelvink method, images are collected in RGB color space, then transformed into a scaled ([0 1]) HSV space (Hue Saturation Value). This value is dependent on the color, degree of saturation and the grayscale value. Once the image is transformed, they group pixels as either 'wet' or 'dry' after histogram smoothing. With the 'wet' or 'dry' HSV characteristics identified, a model was developed that classifies each pixel in the AOI as either wet or dry. In the model, a raw characterization takes place, where outliers are smoothed out with spatial constraints. The edge between the wet and dry zone is marked as the shoreline.

When studying the images collected by the Cape Henlopen system, it is apparent that there are many intertidal bars located on the bay side of the spit producing little shore-break intensity maxima. Therefore, the Aarninkhof and Roelvink (1999) method was selected to identify the shoreline, since it can be applied uniformly to the AOI in every image, regardless of intertidal bars.

In Figure 2.12, as mentioned, it is clear that the dunes toward the north end of the point have been rectified to ground plane, while their elevation is much higher, masking

31

the shoreline at the end of the Cape. This makes it difficult to identify the shoreline in this area of the point. The eastern side of the Cape also has dune fields masking the shoreline, resulting in the decision to identify the shoreline in each oblique camera view, then solve for the (x, y, z) real world coordinates corresponding to the identified (u, v) pixel locations.

Following the Aarninkhof and Roelvink method, a characteristic image from each FOV is selected. The image is a true color (RGB) [1280 x 1024 x 3] matrix, with the first layer identifying the red for each pixel, the second layer identifying the green and the third layer identifying the blue with each value ranging from 0 to 255. This image is converted to a HSV image, with the first layer identifying the hue, the second identifying the saturation and the third layer identifying the value. Each number value in the matrix ranges from 0 to 1. After the conversion, the hue and saturation values for the image are extracted, and plotted as a three dimensional histogram, that is then visually inspected for clustering. The clustering is due to the intrinsic differences between 'wet' and 'dry' pixels, or the fact that pixels associated with water or sand will have different hues and saturations. Once a threshold is determined that can separate the two clusters of pixels, such as a hue value below 0.4 being water (Figure 2.14), this is applied to the image, classifying each pixel as 'wet' or 'dry'. The boundary between the wet and dry pixels is then marked as the shoreline, after visual inspection of the success of the classification scheme (Figure 2.15). The coordinates of this shoreline are easily converted into (x, y, z) space based on the parameters of the system and in-house algorithms set-up for this task. These coordinates can be stored in archives to allow for the change in shoreline to be quantified over weeks, months and years.
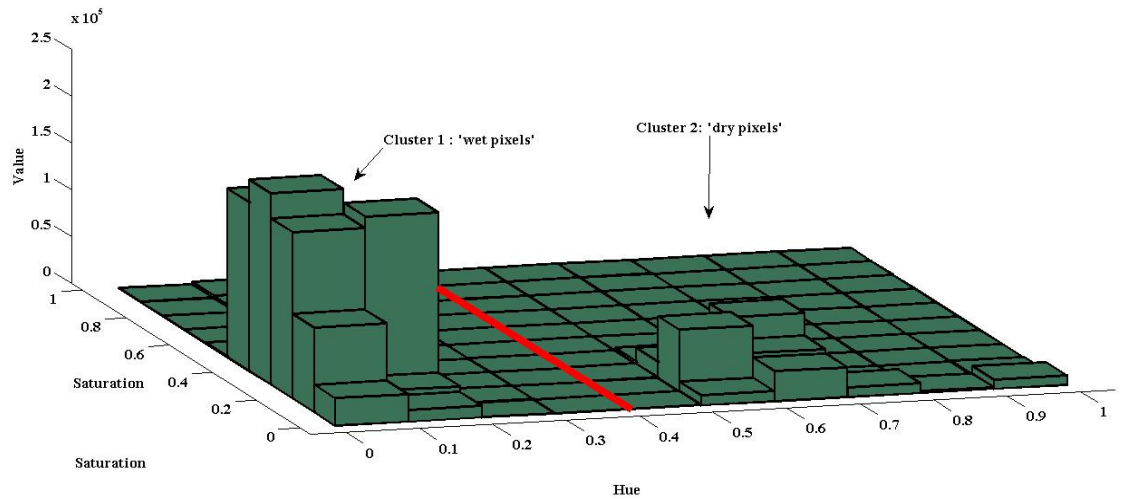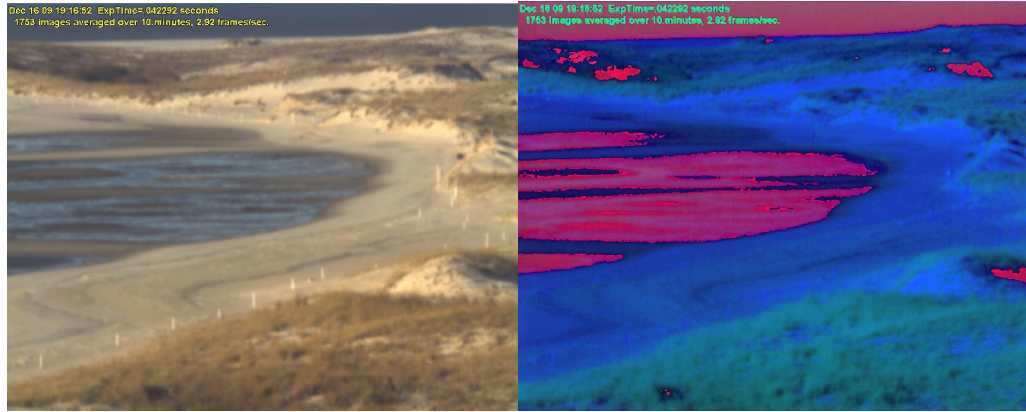
Figure 2.14: The view from camera 6 (top left) at low tide (sand bar features exposed) is transformed into hue-saturation-value space (top right), where the pinks references low hue values and the blues represent high hue values. The pixels in the HSV image are then displayed as a 3-d histogram, where the pixel clustering is very visible. The red line represents the 'cut-off' where points with lower hue values are 'wet pixels' and the points with higher hue values are the 'dry pixels'.

33

Figure 2.15: The contour between the 'wet' pixels and 'dry' pixels has been identified with the blue line in the larger image. Shadow zones in the dune field also have been marked due to having similar HSV characteristics as the wet pixels. The edge between the dune field and the water in the top portion of the image has also been identified, however it does not represent a true shoreline. In order to correct for these miss identified areas, shoreline points will only be recorded in a masked zone, where the shoreline is known to be (subplot).

2.5   Wave Breaker Intensity

In the images collected by the video system, the surfzone appears white due to the bubbles and turbulence caused by wave breaking. With higher turbulence due to waves breaking, the breaker zone appears to be wider and whiter in the images. High energy surf zones are able to suspend, and therefore have the ability (assuming the presence of a current) to transport more sediment than a quiet surf zone, without the characteristic white band in the timex image. With this knowledge, the images on the ocean side of the Cape (that are known to be higher energy than the bayside) are used to observe a potential gradient in the intensity of the breaker zone. This gradient can be indicative of gradients in the suspension, currents and therefore sediment transport along the coast.

From the three ocean facing camera views, images were selected from the same day and hour to analyze. Time averaged images from the early afternoon were used due to uniform solar intensity in the background. Within these images, several (u, v) locations were selected in the middle of the breaker zone, the intensity recorded, and the coordinates transformed into (x, y, z) coordinates for comparison. The intensity, taken from a RGB image, is on the scale [0 255], with 255 representing white, or a high energy, high intensity breaker zone. These geo-referenced intensities, are then plotted (Figure 2.16).

In Figure 2.16, it is observed that the breaker intensity decreases from south to north. This allows the initial hypothesis that the breaker zone is less energetic, with distance north along the Cape. This gradient in energy and sediment transport is a major foundation for the extreme growth on the Cape. However, due to a lightning strike disabling

the cameras, we were unable to determine if this visual gradient in the images is temporally

constant on other days. The cameras will be re-installed in order to complete this objective.

In order to support this hypothesis, in-situ testing of currents was conducted in this region

(Chapter 4).
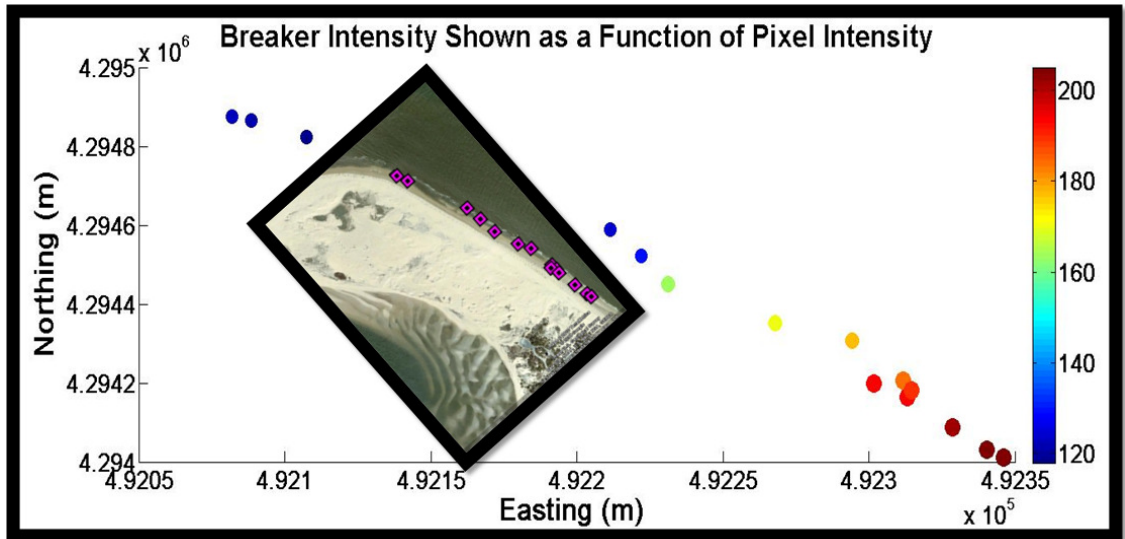
Figure 2.16: The breaker intensity of selected locations along the shoreline is shown in this plot. The selected points (shown in subplot overlaid in Google Earth), are plotted based on their Northing and Easting, with the intensity represented as a color. 255 indicates a pure white pixel, and 0 a black pixel. Therefore, hot colors show whiter, more energetic breaker zones, and the cooler colors, a less energetic surfzone. As you move toward the northern section of the point, the plot indicates a less energetic surfzone, indicative of sediment transport gradients.

Chapter 3

GPS-EQUIPPED VEHICLES AND SURVEYING

To study the changing morphology at the Cape, several GPS-equipped rapid response vehicles have been utilized. These vehicles are capable of robust morphological data with high spatial resolution. The imaging system (Chapter 2) provides two dimensional data of features in the AOI, however is mapped to a level ground plane that cannot provide the third dimension of features such as dunes. The vehicles supply a complimentary data set to the images collected. When morphological data are collected with high temporal resolution, data sets can be used to present quantification of changes in the local morphology due to seasonal variations in conditions, or storm events. The developed vehicles provide rapid response evaluation of the dune field at the Cape, the beach face, and the offshore region. Each vehicle is a unique mechanism for collecting morphology data in a specific region, data that can be merged together to provide a full scale view of the area of interest. The dune field data can be provided from walking with a backpack-mounted GPS, or lidar data provided from the Delaware Geological Survey (DGS) or the United States Geological Survey (USGS). The beach face is surveyed with a GPS-equipped all-terrain vehicle, and the offshore bathymetry is collected with a GPS-equipped personal watercraft. The intertidal zone, having water depths too deep for the all-terrain vehicle, yet too shallow for the personal watercraft, is mapped using a hand pushed re-furbished golf dolly that holds the GPS. Together these vehicles allow us to establish an accurate three-dimensional view of our AOI on the Cape.

3.1 GPS

All of the vehicles have a Magellan Z-max RTK-GPS attached to collect and record position and elevation data. The GPS uses a cellular modem to connect to a network that provides real-time base station data and corrections without the need for a physical base station on location. It also helps provide an easy solution for radio issues between the base station and a roving unit, that were common on the Cape prior to the purchase of a radio modem. The GPS provides very precise measurements (vertical errors are on the order of 2-3 cm and horizontal errors are on the order of 1-2 cm) relative to the ellipsoid.

3.2 All-terrain Vehicle

The all-terrain vehicle used in this study will be referred to as the BSV (Beach Survey Vehicle). The BSV is a Kawasaki Teryx x750 FI 4x4 LI. This vehicle has a rod equipped in the bed of the vehicle that holds the GPS satellite receiver. The rover itself, sits inside the BSV with the driver (Fig 3.1).

Ideally, surveys would occur during low tide, where the maximum amount of beach face is exposed. Surveys can extend from the dune face to about 20 cm of water depth. This allows the BSV to have good coverage of most of the exposed tidal features during extreme low tides. Surveys should be completed at a rate of 8 km/hr. With the RTK-GPS sampling at a maximum rate of 1 Hz, the minimum wavelength of a feature that can be sampled is 4 m.

Due to Piping Plover migration and habitation in the region, the entire north section of the Cape is closed for most of the late spring and summer months. This makes it impossible to survey the full curvature of the point in one pass during closures. There have

been a few successful surveys done of this location (Figure 3.2). The figure shows a

compilation of surveys spanning from December 2009 to September 2010. The one meter

contour has been superimposed on this figure for surveys taken on the following days: 3 Dec

2009, 3 Mar 2010, 5 June 2010, 9 Sept 2010. The December and March surveys highlight

the winter erosion afflicting the Delaware coastline after several Nor-Easters, resulting in a

narrow beach. During the spring and early summer the beach begins to grow wider, due to

calmer wave conditions, as indicated in the June 1 m contour. This growth is even more

evident in the September survey. The September survey was completed a week following

Tropical Storm Earl, a storm that made a close swipe to the Delaware coastline 3 Sept 2010.

Strong waves caused wave run-up to reach the dune foot (Figure 3.3). However, the

September survey shows continued expansion along the coastline, with storm erosion

seemingly not affecting the evolution of the broad summer beach. Once the north section of

the Cape re-opens, surveying can continue throughout the entire Cape coastline, providing

data to allow comparisons between winter profiles in order to determine any long term

erosion or deposition.

3.3   Jet-ski

        The in-house jetski, (Udoo), is the personal watercraft hydrographic survey

vessel (Figure 3.4). It was first constructed in 2008 using the design of (MacMahan, 2001) as

a guide. It provides a low cost vehicle that can be used in shallow depths in the surfzone,

where larger hydrographic surveying boats fail. It is equipped with a motion reference unit

(MRU, brand: KVH) to allow for correction due to pitch roll in the open seas. There is an

echosounder (brand: Tritech) attached at the stern, to record the depth of the water. The

Tritech echosounder, is a single beam

Figure 3.1:   **The BSV, an all terrain survey vehicle.**
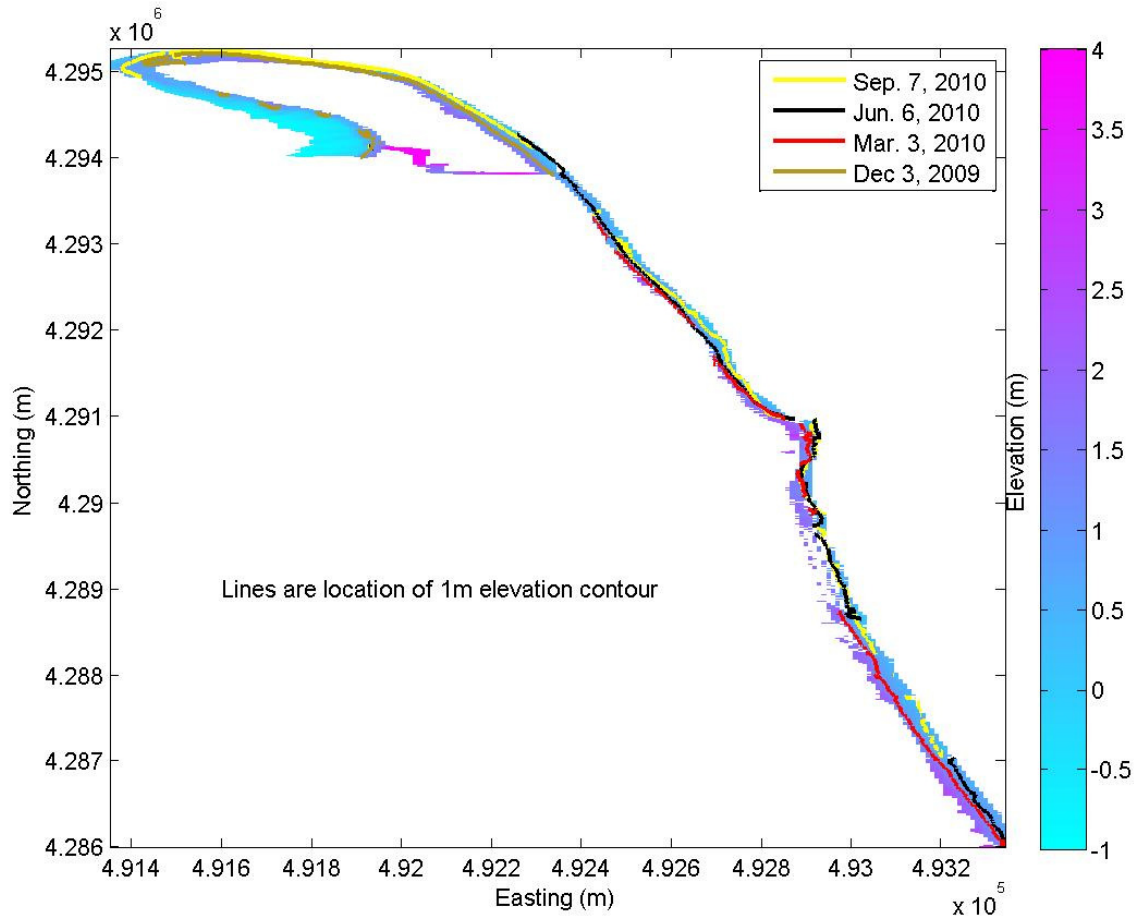
Figure 3.2: A compilation of surveys completed with the BSV around the Cape Henlopen spit, providing the elevation, indicated by the colorbar (m). The one meter contour (pseudo-shoreline) is indicated via a colored line, with: tan, Dec 3, 2009; red, March 3, 2010; black, June 6, 2010; and yellow, September 7, 2010.

Figure 3.3:   **Tropical Storm Earl pounds the Delaware coastline (looking North to the Cape), 3 Sept 2010. Wave run up effected the beach up to the dune foot during the storm.**

Figure 3.4: The Udoo. The personal watercraft hydrographic survey vessel.

sonar, with a 6 ˚ conical beam. The GPS is also attached to the UDoo, to provide the position, recorded along with the depth.

The MRU, echosounder and GPS data are merged through the interface Hypack, a hydrographic surveying software. This allows for depths to be correlated with their position, and corrected with the MRU data, if there is significant wave motion during collection. Hypack also allows for tidal corrections, based on the distance between the ellipsoid (mean sea level height) and the geoid. However for this project, the varying distance between the ellipsoid and the geoid is assumed to be very small, and the distance between the GPS antenna and echosounder measured precisely, therefore the survey vessel is considered a survey rod of fixed length. A computer monitor located near the bow of the vessel allows for the user to view the survey and associated collected data while the vessel is in motion. Once set-up the UDoo provides an accurate method to measure the offshore region of the Cape.

3.4 Dolly

The dolly is a golf caddie that has been re-furbished to have the GPS antenna attached to it (Figure 3.5). With a backpack holding the Rover body inside, and a hand held screen attached to the golf caddie to reference collected data, the dolly allows for the intertidal region to be surveyed. Ideally, a BSV survey would collect onshore data at low tide, a UDoo survey completed to reach most of the bathymetry during high tide, and the dolly to collect any missing data in the overlap between the onshore and offshore data. Traditionally this type of overlap collect is done by a rod and level survey, that can be inaccurate and

spatially sparse. The dolly allows for real-time collection in a grid like pattern, using the same

methods as the other surveys.

Figure 3.5: The dolly surveying intertidal features on the bayside during February field work.

The dolly has been used in particular to survey some of the bayside tidal features located at the Cape. The focus has been an individual bayside feature where sensor deployment was located (Figure 3.6; Section 4). Surveys have found the dolly is capable of working in depths up to a 1.5 m of water. Surveys were completed in February, June and September of 2010, providing a dataset showing the short term development of the feature between the winter and summer seasons (Figures 3.7). Overall, between February and September, the feature has higher elevations indicating growth and deposition in the region. The highest rates of deposition are near the southern side of the feature, hinting at a southerly migration, however additional surveys would be valuable in order to determine how the evolution relative to a year of seasonal storms and wave conditions. The sensor deployment and results can be found in Section 4.2.

Figure 3.6: The location of the surveyed feature (inside red box) on the bayside as overlaid on a Google Earth image.
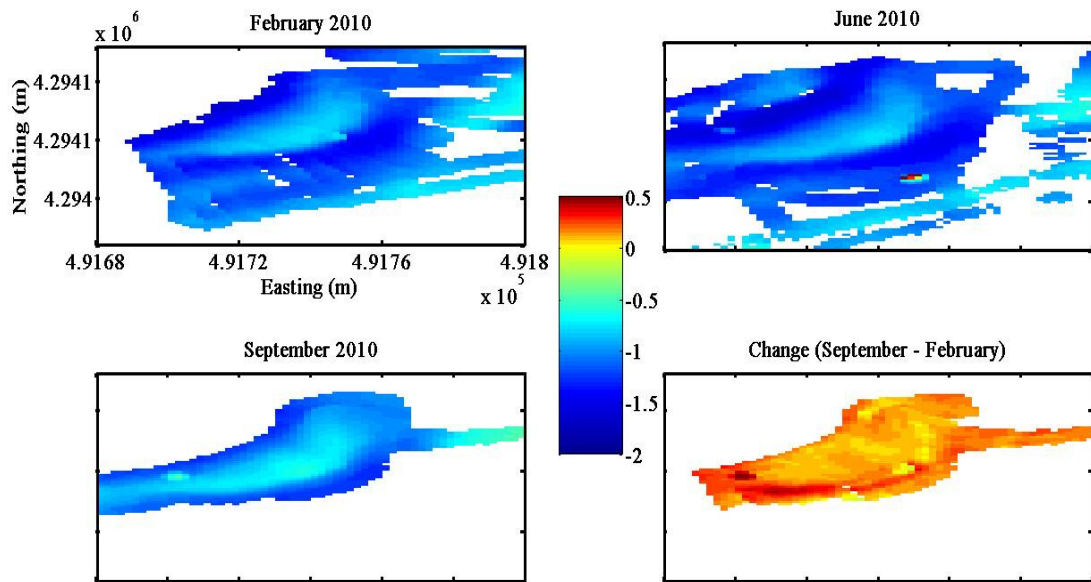
Figure 3.7: Surveys of a bayside feature: February 2010, June 2010 and September
2010. The bottom left figure shows the change in the elevation of the
feature between February and September, with hotter colors showing
deposit

51

Chapter 4

SENSOR DEPLOYMENT

The Cape is the location of a unique morphological and hydrodynamic situation. With the Cape at the mouth of the Delaware bay, it experiences affects from the tidal currents flooding into the bay, and ebbing out. The Cape also encounters influences from Hen and Chickens Shoal, a submerged bathymetric feature that forms at the tip of the Cape, running roughly parallel along the northerly portion of the Delaware coastline (Figure 4.1). The configuration of the bay, Cape and shoal allow for an interesting question to be raised. Is there a persistent northerly current found at shoreward of the shoal due to recirculation and shear currents during the ebb tide? Would this explain the exaggerated growth observed at the Cape? An initial exploration of the currents along the northern Delaware coastline with the use of current meters and pressure sensors was implemented in two locations on the Cape, for 72 hour periods, in order to study this question. The first sensor deployment was completed on the previously mentioned (Section 3.4) bayside feature in order to test the set-up of the sensor configuration in February 2010. An ocean side deployment was completed in June 2010, in order to study the prevailing currents in the region.

4.1   Instrumentation

The sensors used in the field deployments are Druck pressure sensors and ValePort electromagnetic current meters. The pressure sensor allow for the water depth, and, at a high sampling frequency, wave height to be calculated. The current
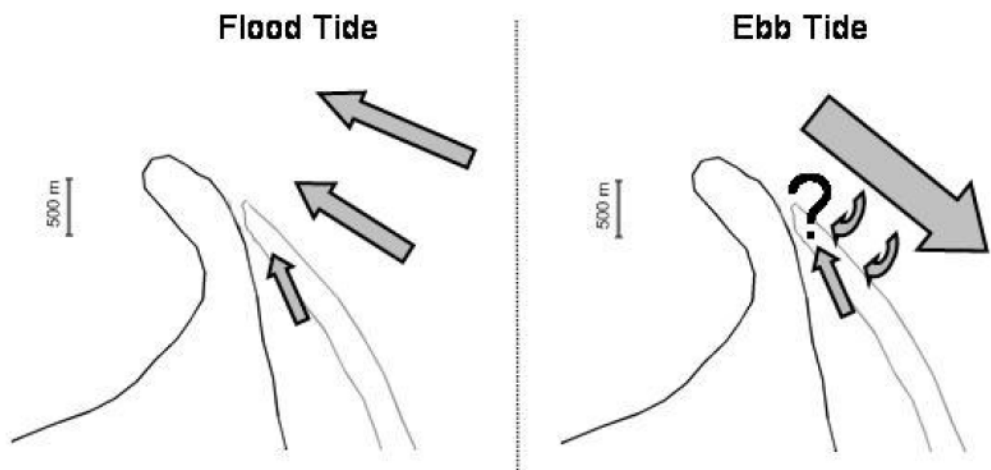
Figure 4.1: A schematic of the Cape, and Hen and Chicken Shoal with hypothetical tidal effects. During flood tide, the prevailing current is to the north. It is thought that during ebb tide, recirculation affects may also cause a north directed current, resulting in a constant northerly current.

meters provide current velocity data, with hopes of determining tidal current magnitude and direction. The sensors are situated on a 1.5 m steel tripod (Figure 4.2). The tripods (6 in total) are deployed in pairs, with one tripod housing a data logger, and a battery providing power, connected to the other tripod via 20 m cables.

In order to place the tripods at the greatest depths possible, all deployment is done at extreme low tides, with calm wave conditions, where they will remain for multiple tidal cycles. During deployment, the tripods are configured on the beach, then carried out to location where they are jetted into place, via anchors in the sand using a centrifugal pump. Once secure, the tripods can be left in the intertidal zone for several tidal cycles as they collect data (Figure 4.2).

4.2   Bayside Deployment

In February 2010, 6 tripods were deployed on the studied bayside feature (Section 3.4; Figure 3.6), with data collected for 2.5 days. The tripods were set up with three on the elevated section of a crescent shaped feature, and three in the trough surrounding the feature. This feature is the final bar of sand in the tidal zone exposed at low tide, and its southwestern side is exposed to the open bay. The current meter data was normalized for orientation, and plotted over the location of each sensor (Figure 4.3). The flood and ebb tides were classified based on water depth gathered from the pressure sensor during collection. The mean current is shown in the plot, as the semi-major ellipsoid axis, and the standard deviation of the flow is show as the semi-minor axis.

The three current records for tripods located on the feature (1, 3, 5) are most likely wave dominated, due to their placement in shallower, with standard deviations on the order of their mean current signal. Sensors 1 and 3 are at the highest elevations, and are experiencing water encroachment from all sides during flood tides (and vice versa during ebb tides), adding to the disorganized velocity signal. Tripod 5 is located at a lower elevation, with a tidal flat to its northeast, providing a more organized tidal signal, directed toward the higher elevations on the feature. The deeper tripods (2, 4, 6), show a more distinct velocity signal, in particular during ebb tide. Current meters 4 and 6, show ebb tidal currents with an perceptible direction and lower standard deviation. They illustrate the water draining off of the surrounding features as the tide ebbs out of the bay. Sensor 2, exposed to the most undisturbed bay tidal currents, has tidal signals oriented in alignment with the expected tidal patterns seen by the bay as a whole, and is likely less affected by waves and drainage off of the feature. The deployment of the sensors on the tripod was successfulallowing for an ocean deployment.

4.3   Ocean Deployment

In September 2010, a field deployment occurred on the ocean side of the Cape, with two tripods deployed at a distance of 1 km from each other. They were placed in the intertidal zone during a very low spring tide. The sensors collected data for 14 hours, capturing a full tidal cycle. The water depth and current meter data were corrected for height above bed level and orientation, respectively. Based on the plot (Figure 4. 4) there appears to be a 20 minute lag between the max water depth, and the

55

Figure 4.2: Tripod deployment. A: A view of several tripod being prepared for deployment. B: Optical backscatter sensor (left; not utilized) and pressure sensor (right) attached to a tripod. C: Current meter attached to tripod. D and E: Tripods placed on the bayside bathymetric feature, at extreme low tide. F: As the tidal wave enters the bay, the tripods begin to be covered with water. At high tide they will be complete submerged.
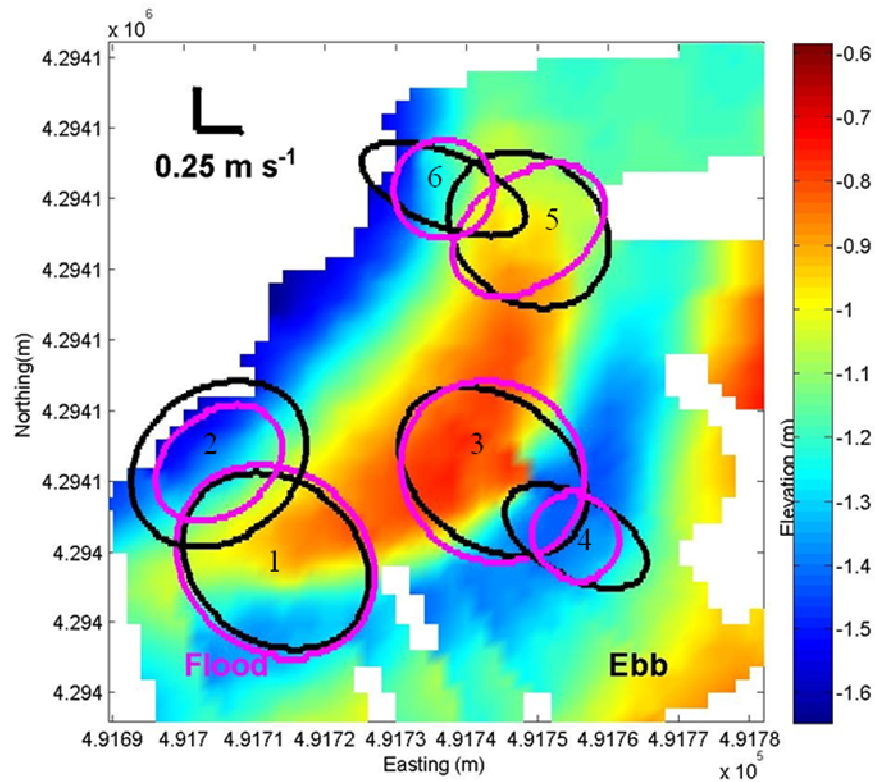
Figure 4.3: The data collected from the six current meters are shown above relative to their surveyed locations on the feature. The elevations (m) are indicated in the colorbar. Flood and ebb tides have been separated based on the water elevations collected by the pressure sensor. The ellipsoid semi-major axis indicate the mean current signal, with the semi-minor axis indicating standard deviation, and each ellipsoid is centered over its corresponding sensor. The scale representing the magnitude of the signal is shown in the top left portion of the figure, in m s^{-1}. Each tripod (1-6) is numbered.

tidal velocity reaching zero. This can be correlated to the prevailing waves from the south, giving the alongshore current an additional push to the north, before switching over to a tide-dominated south current during ebb tide.

This influence would also explain the discrepancy between the maximum velocity during flood tide and ebb tide. During flood tide, the current meters record a maximum velocity (to the north) of 0.7 m s^{-1}, however only record a maximum of velocity (to the south) of 0.3 m s^{-1}. Interestingly, the southern current meter has a lower overall magnitude of velocity than the northern current meter; this is not the gradient in alongshore current that would indicate a northerly sediment transport and deposition. However, it is evident that during collection, the northerly current was much stronger, supporting northerly sediment transport. It is noted that the southern current meter was located 10 cm above the bed while the northern current meter was located 20 cm above the bed. This may explain some of the discrepancy in the velocity between the two.   This initial exploration into sensor deployment begins to hint that there may be a stronger northerly current in the region, however without further experimentation and data collection during different times and conditions, we are unable to conclude this influences the exaggerated growth at the Cape.
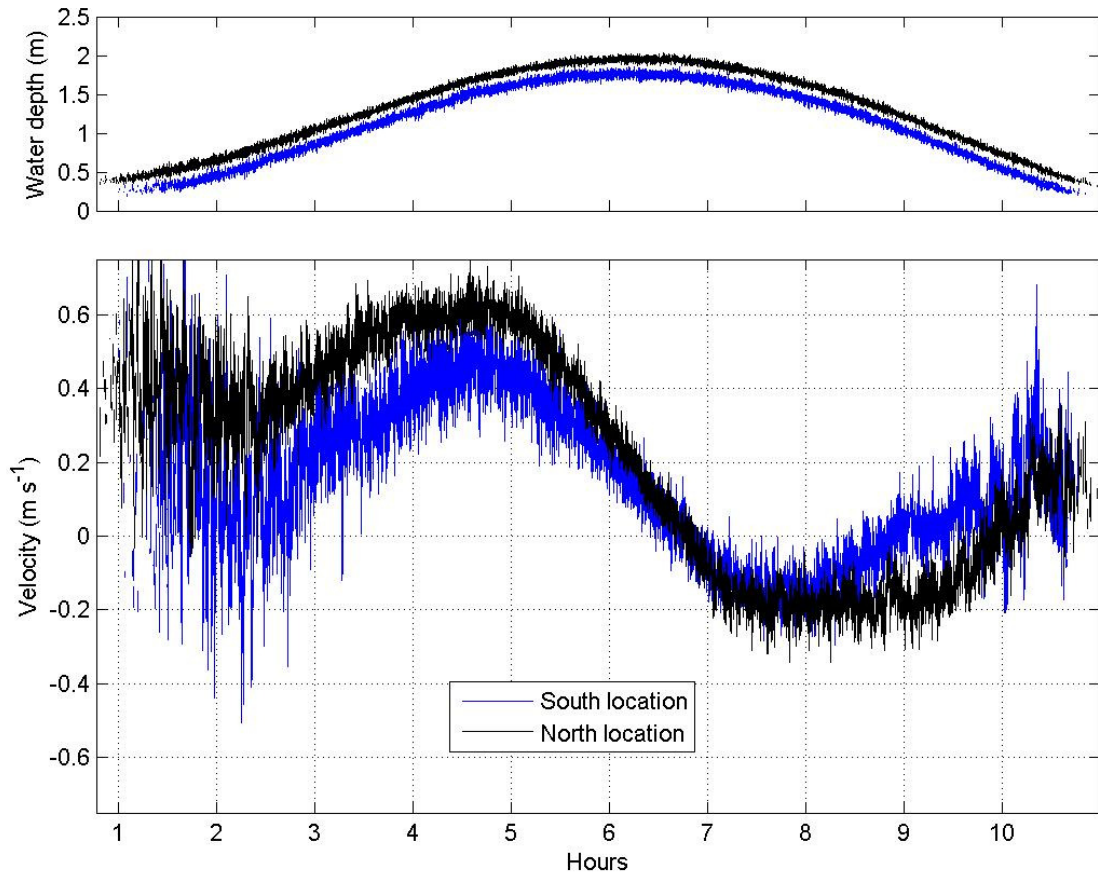
Figure 4.4: Data collected at on the ocean side with the tripods. Blue indicates the south location and black is the north location. The top figure shows the water depth in meters (note the 20 cm discrepency between the north and south water depths). The bottom figure shows the velocity recorded in meters per second. There is ~20 minute lag between high water and a velocity of 0 m s^{-1}.

Chapter 5

MODEL SIMULATION

Once in-situ data has been collected, it becomes important to use numerical simulation to help support field observations. Numerical simulation allows for theories made based on the field observations to be tested, while controlling the conditions that the AOI is exposed to. The ultimate goal of the studies on the Cape is to better understand the morphological response to the different hydrodynamic conditions in the AOI. A major interest is evaluating the results produced by a robust numerical model at the Cape during tropical storm event. This is a period of time believed to produce significant morphological change. Northerly currents produced by the storm may help explain the rapid growth at the Cape, sending sediment toward the tip of the point.

Several modeling approaches exist, including those that resolve geologic details of underlying sediment, but do not resolve individual storms (Cowell 1995, Rosati 2010, Stolper 2005), to those that resolve the coupled interactions between topography, waves, currents, and sediment transport (Cañizares 2008, Lesser 2004, Roelvink 2009, McCall in press). In order for detailed models to be useful, it is important to demonstrate the realism of simulations of specific storm events. Simulations should correspond to sensible, if not quantitatively accurate, predictions of actual storm scenarios. Previous detailed models (Roelvink 2009, Jimenez 2006, McCall in press, van Thiel de Vries 2008) have focused on barrier islands with relatively high dunes where storm-driven overwash is an important process, similar to the Cape, although, the Cape is not a barrier island.

A recently introduced numerical model, XBeach (eXtreme Beach behavior model), implements morphological modeling of dune erosion, overwash, inundation, and breaching (Roelvink et al., 2009). Roelvink et al. (2009) demonstrate that the model skillfully simulates storm hydrodynamics including short- and long-wave heights and associated currents as well as predicting sediment transport associated with dune erosion. In particularly, they demonstrate that the model can recover observed variations in dune erosion associated with storms that struck Assateague Island on the U.S. east coast. The variations in erosion response depended on variations in the initial topography, that ranged from relatively high dunes (>4 m) to relatively low dunes (< 2 m). These storm conditions were spatially homogeneous, with storm surge elevations close to 1 m and offshore wave heights of about 4 m such that dune overwash occurred where the dune height was less than about 2 m. This study indicated that variations in the storm conditions (i.e., surge height, wave height, and wave period) could also control the degree of dune erosion, primarily by increasing or decreasing the intensity of dune overwash.

The model is an open source, making it easily available for our study of the Cape. Unfortunately, there currently is no elevation data pre- and post-Nor'easter in the region to determine if the results are fairly accurate in the magnitude and location of the simulated morphological change. A conglomerate of lidar and bathymetry data is available (lidar data from DGS, 2005 and NOAA bathymetry from the late 1800's to 2000) for a study, however without pre- and post-storm data for model comparison, it become impossible to determine the robustness of the model.

To determine XBeach's success in such a venture, a location with pre- and post-storm morphology data, hydrodynamic conditions and a large storm needed to be selected. Cape Henlopen does not have a data set that is as dense or robust as needed for

such an evaluation. Still, an initial study, to determine XBeach's skill in modeling

morphological change due to extreme hydrodynamic conditions, must be done in

preparation for a future exploration at the Cape. For this, in conjunction with the USGS's

Extreme Storm Group, the Chandeleur Islands, a barrier island chain in South East Louisiana

was selected to study under the extreme hydrodynamic conditions produced by Hurricane

Katrina, where an comprehensive data set is available. This study will provide insight into

how well this relatively new model performs, in order to determine its appropriateness for

Cape Henlopen. After the description of the test simulation at the Chandeleur Islands,

preliminary set up and results from a simulation for the Delaware coast will be presented

along with future plans for a vigorous model study at Cape Henlopen.

5.1   Model Background

XBeach is a coupled hydrodynamic and morphodynamic model that can be

used to test a range of morphological modeling concepts and resolve processes at relatively

small spatial, $O(1\ m)$, and temporal, $O(1\ s)$, scales. It is capable of handling extreme

conditions, including hurricanes. Processes that are resolved by the model include wave-

averaged evolution of short waves, time-resolved evolution of long waves, wave-driven

flows, sediment transport, and morphological change. For an in-depth description of

XBeach, see Roelvink et al. (2009). For the purposes of this study, we require a

morphological prediction that depends on hurricane-driven processes.   Morphologic change

is obtained from XBeach from the sediment mass conservation equation, wave- and flow-

driven sediment transport parameterizations, wave-energy conservation, and momentum

conservation.

A key formulation in the morphological evolution problem includes a formal separation of the fast time scales associated with hydrodynamic processes and the relatively slow evolution of the morphological features of interest. This separation makes it possible to decrease computational time. This is done by using a time scale multiplier, or morfac, to sample the hydrodynamic inputs and to apply a multiplier to the morphologic response. This is implemented as

$$\frac{\partial z}{\partial t} = -\frac{m}{(1-p)}\left(\frac{\partial q_x}{\partial x} + \frac{\partial q_y}{\partial y}\right), \quad (2\ )$$

where z is the spatially and temporally varying bed elevation, q_x and q_y are the corresponding sediment transport rates, p is the sediment porosity (0.4 for this simulation), and m is the adjustable morfac parameter that separates morphological and hydrodynamic time scales, in order to speed up morphological response. The implementation allows the hydrodynamics to be computed on a fast time scale, Δt, but the morphology and boundary conditions change slowly, with a time step of $\Delta\tau$, where $\Delta\tau = m\,\Delta t$. To implement this consistently, the boundary conditions (i.e., wave parameters and water levels) are updated using the large time step as well. So, for example, at the nth computational time step, the fast hydrodynamics are computed and stored at t_n $(= n\,\Delta t)$ while the bed level is computed and stored at τ_n $(= n\,m\,\Delta t)$. Boundary conditions, B_n $(=B[\tau_n])$, are sampled from the input time series with this larger time step, $\Delta\tau$. If, for $m>1$, bed level and boundary condition changes are indeed small at the short time scale, then this approach should yield an accurate approximation of the short-scale averaged morphological response. Implications of this approach include sub-sampling the boundary conditions and altering the coupled model feedback mechanisms. Lesser et al., (2004) discuss these effects in an application to another

numerical model. The sole benefit of the approach is to reduce computation time for a problem that spans a broad range of time scales. For example, a simulation that takes 50 hours to run with $m = 1$, would take 5 hours using $m = 10$.

The sediment transport formulations are described by Roelvink et al. (2009) and McCall (in press). A depth-averaged advection-diffusion scheme with source and sink terms is used to model sediment concentration in the water column, varying on the long-wave time scale. The sediment transport formulations are applied to a single sediment type that is defined by grain-size and density parameters. As is true with most study sites, the Chandeleur Islands contain numerous sediment types, including marsh, mud, peat and sands, each with unique transport rates. We will address this model-implementation limitation in the discussion.

The flow model is based on the nonlinear shallow water equations at a time scale that resolves long waves forced by wave groups but not individual short waves. Wave-averaged equations are used to determine the short-wave energy conservation given offshore boundary conditions that resolve wave directional distributions while assuming a narrow-banded frequency spectrum. Wave energy dissipation is fed to a roller model, and roller dissipation results contribute to radiation stress gradients that force slowly-varying currents.

5.2   Study Site and Model Domain

The Chandeleur Islands (Figure 5.1), showing the northern portion of the islands), are part of the Breton National Wildlife Refuge, and are located 161 km east of New Orleans, Louisiana. They form an 80 km long barrier island chain in the Gulf of Mexico and

are oriented roughly north to south. The Chandeleurs are remnants of the St. Bernard Delta, formed by the Mississippi River. The islands are a significant feature in the gulf that may represent the fate of a dying barrier island; being one of the most rapidly receding island systems in the United States (Kahn, 1986). The topography in some areas is extremely low, with elevations in our focus region that were uniformly less than 2 m.

During the hurricane season of 2005, the islands were impacted by several hurricanes, most notably Hurricane Katrina. This hurricane is one of the costliest storms, in both fatalities and damage, to ever make landfall in the United States. It struck the Atlantic coast of Florida as Category 1 on the Saffir-Simpson Scale. It then crossed the Florida peninsula into the Gulf of Mexico and rapidly strengthened to Category 5, before making landfall as a Category 3 west of the Chandeleur Islands (Knabb, 2005). The high storm surge and strong waves resulted in island fragmentation with numerous breaches that exposed wetland once protected by beaches and dunes. Based on comparisons of lidar surveys, approximately 82% of the island area was lost between 2002, just after Hurricane Lili, and 2005, just after Hurricane Katrina (Sallenger et al., 2009).

Figure 5.2 shows satellite imagery of the evolution of the islands from 2001 to 2005, and the development of the islands from a continuous chain to a highly disconnected group. The islands during this time period were battered by hurricanes Lili (03 Oct 2002), Isidore (26 Sept 2002), Ivan (16 Sept 2004), Cindy (05 Jul 2005) and Katrina (29 Aug 2005). The storm tracks of these hurricanes are highlighted in Figure 5.1. It is obvious that in several locations the islands completely disappeared (north section of islands) and sediment was washed away throughout the chain, leaving only marshland (Figure 5.2).

The model domain used is a 4 km x 4.5 km section of the islands (Figure 5.1). The domain uses a grid resolution of 20 m in the alongshore direction and a spatially varying cross-shore grid resolution that ranges from 20 m offshore to 10 m in the area of interest around the islands. Discussion of the choice for resolution is given in Section 5.7. The boundary conditions applied to the model include wave height, direction, and peak period on the gulf-facing offshore boundary.   Additionally, four storm surge elevation time-series were applied at each corner of the domain and interpolated alongshore to constrain the seaward and landward boundaries for the duration of the simulation. The hydrodynamic conditions used are discussed in Section 5.3. The initial bed elevation was obtained from a smooth interpolation of the pre-storm lidar data and offshore bathymetry (Section 5.4).

5.3   Hydrodynamic conditions

Forcing conditions were provided by the United States Army Corps of Engineers (USACE). Data included wave, water level, and flow inputs (Figure 5.3). Significant wave heights were simulated using the STWAVE model (Smith et al., 2001) driven by the hurricane wind field. The spatial resolution used in STWAVE was 200 m. STWAVE was forced at the offshore boundary by the WAM model with 30 s temporal resolution. Water levels and velocities were simulated using ADCIRC (Luettich et al., 1992), which was driven by the wind and the wave fields. These models have been used for post-storm analysis by the USACE in comparing the outputs from the STWAVE and ADCIRC data set to observational data collected during Hurricane Katrina (IPET, 2007). Prediction errors for STWAVE ranged from 0.1 to 0.3 m under prediction of wave height during the storm peak in the inland waters of Lake Pontchartrain. Errors were less than 1 m in the domain just offshore of the Chandeleur Islands. Extensive comparisons can be found in the IPET report. ADCIRC

predicted storm surge was strongly correlated with observed high watermarks (R^2=0.82) and, on average, under predicted the elevations by 0.18 m (IPET, 2007).

Model data from STWAVE, ADCIRC and observational data obtained from NOAA gages 42007 (near the north end of the Chandeleur Islands, (Figure 3) and 42040 (offshore) and two tide gages (Waveland, MS and Mississippi Pilot Station East) are consistent. Modeled values were extracted from three different locations (named ADCIRC/STWAVE 1,2,3) that were relatively close to the observation locations (Figure 5.3). The predicted storm surge at all locations was similar to the observations before the storm peak, prior to failure of the Waveland gage. The predicted surges at the Chandeleur Island locations far exceeded the measurements, but this is consistent with the previous analyses of the actual spatial patterns of observed storm response (IPET, 2007). Wave height, period, and direction at ADCIRC/STWAVE 1 compared well with observations from gage 42007, (Figure 5.3). The gage failed before the storm reached its peak, so we include comparisons to the offshore gage. Predicted wave heights were different, as expected, while wave periods compare well with those from the offshore gage throughout the duration of the simulation. At the offshore location, wave directions near the peak of the storm approach from a southwesterly direction, differing from the model predictions near the Chandeleurs. This is likely due to the differences in the geographic settings, since the Chandeleurs do not receive ocean waves from the west.
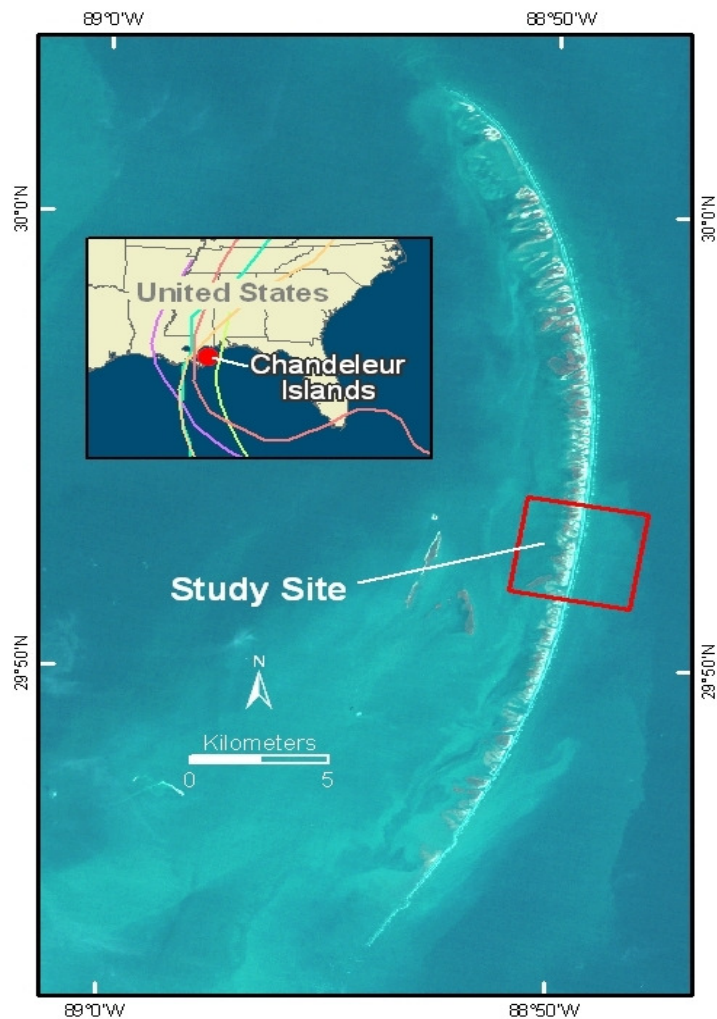
Figure 5.1: Chandeleur Islands, study site highlighted in red box. Recent hurricane tracks are shown in the inset, with: Purple- Lili (2002); Aqua- Isadore (2002); Green- Ivan (2004); Beige- Cindy (2005); Pink- Katrina (2005). (Landsat satellite imagery, 2004)
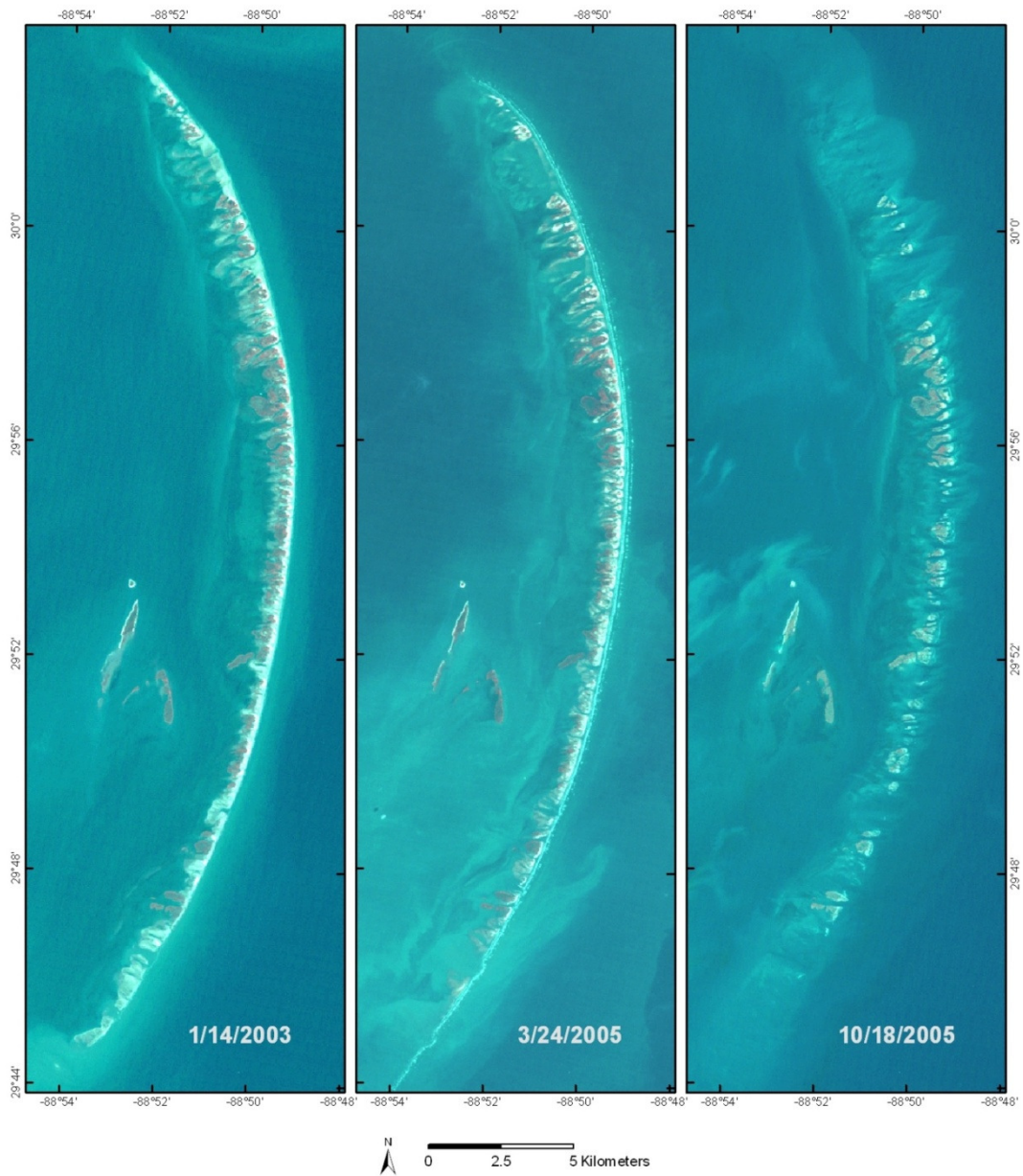
Figure 5.2: Recent hurricane effects on the Chandeleur Islands. (Landsat satellite imagery)

Hydrodynamic predictions from ADCIRC at the locations matching the onshore and offshore boundaries of the XBeach domain were used as XBeach water level boundary conditions. Flow velocities were not used in the simulation. The wave information from STWAVE was used to produce a parameterized Jonswap spectrum of the short wave information to XBeach. These data were applied only to the offshore boundary, with no waves being forced from the back bay (west) region. Incident waves from the back bay region were probably seen during the storm, however they can be considered secondary waves with a much lower impact than the waves forced from the east. The model was forced from 28 Aug 2005 00:00 to 30 Aug 2005 12:30. Storm surge elevation reached a peak value of 3.5 m. The peak significant wave height was 5.7 m with a mean wave period of 12.7 s (Figure 5.3). The mean wave direction was initially 110 nautical degrees as the storm approached the islands, rotating to 135 nautical degrees as the storm left the Chandeleurs.

5.4   Bathymetry

Bathymetry data used to initialize the bed level was produced using a fusion of airborne lidar topography and ship-based sonar bathymetry. The most recent lidar survey prior to Hurricane Katrina was completed on 18 Oct 2002 after Hurricane Lili struck the island and was collected using NASA's Airborne Topographic Mapper, ATM, (Brock et al., 2002). There were several hurricanes that affected the region in the time between the initial lidar survey and Hurricane Katrina. Although this results in a discrepancy between true pre-Katrina topography and the initial topography input to the model, it is the best available data. The bathymetry input for the study site
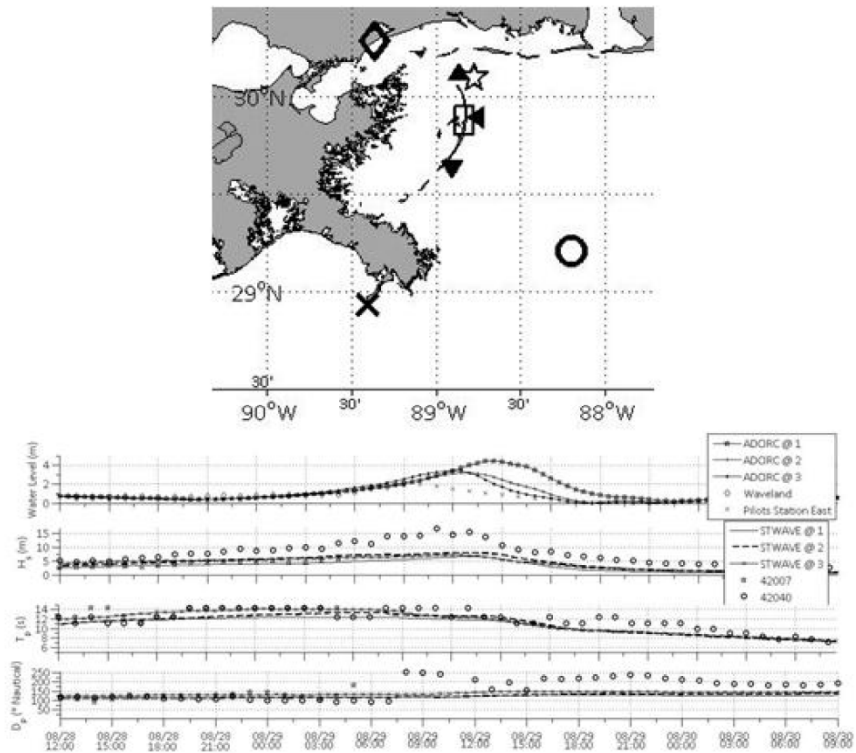
Figure 5.3: Location of forcing condition inputs (top panel). The study site is boxed. Locations are: ADCIRC/STWAVE 1 ▤, ADCIRC/STWAVE2 ▤, and ADCIRC/STWAVE3 ▤. Tide gage data locations are: Waveland ▤, and Pilots Station East x. NOAA wave gage data was collected at two locations denoted by a star (gage 42007) and an open circle (42040) Forcing conditions used for the study site during Hurricane Katrina (lower panels). The forcing variables from top to bottom are are water level, significant wave height (H_s), peak wave period (T_p), and mean wave direction (D_p).

required inclusion of offshore bathymetry data that was sampled in 2006 and 2007 (Twitchell et al., 2009). These data post-date Katrina's landfall, but our assumption is that discrepancies in the offshore region will have minimal impact on the waves and water level prediction over the island itself. This assumption is supported by Roelvink et al. (2009) who showed that morphologic response was not sensitive to substantial variations in the submerged foreshore slope. Lidar and bathymetry data were assimilated using spatial interpolation that included smoothing and also enforcement of minimum gradients on lateral boundaries (Plant, et al., 2002; Plant et al., 2009). The initial interpolation included both the lidar and bathymetry data, interpolating them to a coarse resolution (100 m cross-shore, 500 m alongshore) domain. The data were weighted according to assumed uncertainties:

$$\sigma_{bathy} = \varepsilon_{bathy} \, \exp\left(\left[\frac{z_{bathy} - z_0}{d_{bathy}} \right]^2 \right), \quad (3)$$

$$\sigma_{LIDAR} = \delta_{LIDAR} + \varepsilon_{LIDAR} \, \exp\left(\left[\frac{z_{LIDAR} - z_0}{d_{LIDAR}} \right]^2 \right) \quad (4)$$

where ε_{bathy} (10 m) are possible elevation errors due to changes in the island topography, z_0 (0.0 m) are elevations where these errors are maximum, d_{bathy} (2 m) is a decay scale to control where the errors become negligible (i.e., at depths of about three times d_{bathy}, the bathymetry data are assumed to be error free). Likewise, lidar errors result from expected system errors (ε_{lidar}=0.15 m) and error associated with lack of penetration of the laser to the bottom (ε_{lidar}=10 m and d_{lidar}=1m). These formulations generally allow bathymetry to

dominate the interpolation in deep water (depths greater than 1-2 m), and allow the lidar to

dominate the topography. A second iteration of the interpolation scheme created a high

resolution bathymetry (10 m cross-shore and 20 m alongshore) using the lidar data alone

and updating the low resolution "prior" estimate. The high resolution result was identical to

the low resolution where there was no lidar data. It reflected the detail of the lidar data at

higher elevations and transitioned smoothly into the bathymetric data.

Post-storm lidar data were collected on 01 Sept 2005. Because these data

were not used as model input, it was not necessary to assimilate the bathymetry data.

Instead, spatial interpolation was used to filter spurious measurements. Unreliable

interpolation estimates were rejected if sample errors describing ability to reduce noise,

exceeded 25 % (Plant et al., 2002), or root-mean-square (RMS) errors (describing lidar

clutter) exceeded 0.5 m. Ambiguity associated with distinguishing low-lying topography

from the sea surface required using additional information from color-infrared satellite

imagery to classify land and water. The classification was trained over manually selected

patches of land and water that determined the correlation of three color channels (red,

green, blue) to either land or water. The classification was imperfect and returned

information on its uncertainty so it was, in turn, assimilated with the interpolation elevations

as follows. Data were rejected if the imagery strongly contradicted the topographic data.

That is, data were rejected if the image classification was confident that the scene included

water but the elevations exceeded -0.5 m. Likewise, data were rejected if the classification

was confident that the scene included land, but the elevation was below -0.5 m. The post-

storm topography that survived the assimilation with the imagery (Figure 5.4) was used to

assess the model simulation's predictive skill.

5.5   Results

The conditions chosen to represent Hurricane Katrina caused inundation for a majority of the simulation period at the study site. Maximum water levels over the island were almost 4 m above mean sea level. Given that initial island heights in the study region were at most 2 m, the island would have been inundated even if it had not suffered from erosion. Based on the observational data, it is apparent that the island was breached in numerous locations and that the island elevations were greatly reduced in the regions that did not breach (Figure 5.4). Within the XBeach model domain, the observations indicate that 90% of the island area with elevations above mean sea level was lost between 2002 and 2005; all of the area with elevation exceeding 0.5 m was lost; and 80% of the area with elevation above -0.5 m was lost (based on comparing lidar surveys between these time periods).

The simulated post-Katrina topography is shown in Figure 5.4. The data mask used to filter the initial topography was used to filter the simulated topography so that visual comparisons can be made where the original data were accurate. The simulated morphodynamics eroded higher topographic features and tended to smear them in the cross-shore direction and increased the amount of island dissection. While the simulated elevation-lowering and dissection is qualitatively consistent with the observations, the simulation did not produce the same degree of dissection and island lowering that is apparent in the post-storm observations. Many of the areas that appear as only nearly-breached in the XBeach results correspond to regions that were actually converted to open water (shaded blue in the post-storm survey map). The mean simulated elevation change over the island was about 0.06 m (erosion), and the maximum simulated erosion was about 1 m where incisions cut through the highest topography.

74
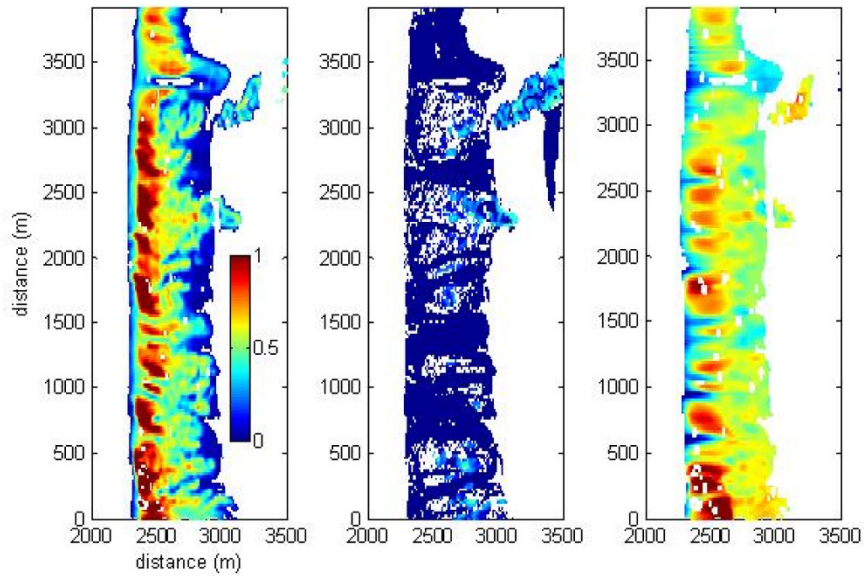
Figure 5.4:   Topography from the initial survey (left), post-Katrina survey (middle), and post-Katrina simulation (right). Data were masked (blank areas) where there was poor lidar coverage or sample root mean square variance exceeded 0.5 m or lidar elevations were inconsistent with image interpretation. Post-Katrina topography that converted to open water (based on image analysis) is shown as "deeper" regions—the actual depth in these areas is unknown.

We investigate in more detail the correlation between observed and simulated changes. In Figure 5.5, the observed change, (the difference between lidar-surveyed initial and final topography) is plotted against simulated change (the difference between XBeach initial and final topography). A perfect correspondence between observation and simulation is indicated by the dashed line. Points below and parallel to this line show that the simulated erosion is correlated to the observations. An offset relationship is apparent, where the post-storm elevation is under predicted by 0.5 - 1.0 m. The under prediction may be explained by the fact that the initial topographic data significantly pre-dates (by three years) Katrina's landfall as it is apparent that there was substantial pre-Katrina evolution (Figure 5.2). This possibility will be addressed in Section 5.9.

More information for this analysis was extracted by utilizing the image-based classification of land and water associated with the post-storm topography (no bathymetry was available for comparison). Points marked with black in Figure 5.5 represent locations where the observed topographic elevations from lidar were above the mean water level both before and after Katrina. Grey points represent locations where elevations were observed to be above mean water level prior to Katrina and were below mean water after the storm—i.e., they were converted to open water. To make this comparison, the post-storm elevations of regions that were under water were assumed to be at least at the mean water level. We created an augmented elevation model with the missing data replaced with 0.0 m elevation. Thus, if a grid elevation from the pre-storm survey was 2.0 m and the final elevation was missing, but clearly submerged, then an augmented "observation" based on the imagery would indicate 0.0 m elevation. The "observed" elevation change would be estimated as -2.0 m and would likely be an underestimate of the true change. However, it

76

allows us to determine if the model can accurately predict the locations of severe erosion. This classification of the results indicates that the simulated changes were correlated to the observations (R^2=0.42) when there were large enough changes to convert topography to open water. Topography that survived on the landward side of the island was observed to erode. However, the simulations predicted little or no elevation change and these predictions were not correlated to the observations (R^2=0.02). Further discussion of the statistical analysis can be found in Section 5.9.

Figure 5.6 describes in more detail the differences between the observed and modeled changes. Observed erosion includes removal of grass-covered berm (labeled *brm*) at the back of the beach (*bch*) and island lowering across the entire barrier platform. Vertical exaggeration makes the beach appear as a steep slope. Its actual slope is about 1:50. The model predicted the berm erosion as well as some profile migrations that were below the mean water level (and thus, not observable in the post-storm lidar survey). Landward of *x* = 2800 m, prominent features are recognizable in both pre-storm and post-storm photographs, in the lidar map, and in the elevation cross-section. This suggests that there was little erosion or deposition at the landward side of the island. Specifically, there was no evidence of overwash deposits in either the observations or model simulation. Island response in this scenario is different from the results of previous studies that focused on overwash-driven sediment transport. Figure 5.7 shows the elevation changes over the full study area that were both observed and simulated. Observations suggest that erosion occurred over the entire island surface—there was no deposition. In the simulation,
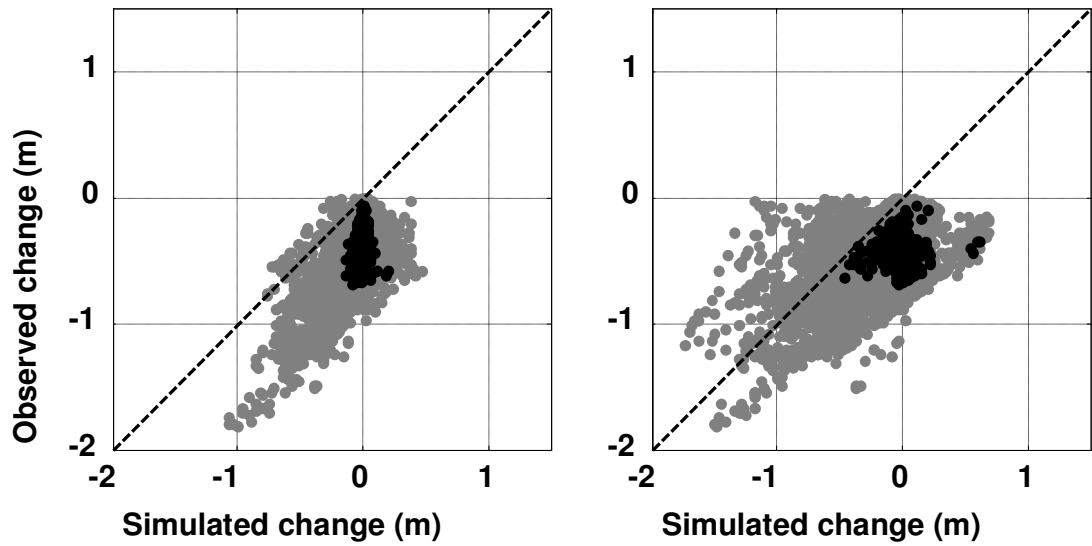
Figure 5.5:   Comparison of observed and predicted changes. The changes are shown for simulation of a single Katrina storm (left) and simulation of four consecutive storms (right). The black symbols represent locations where observed topographic elevations were above the mean water level both before and after Hurricane Katrina. The gray symbols represent locations where observations indicate that topography was converted to bathymetry.
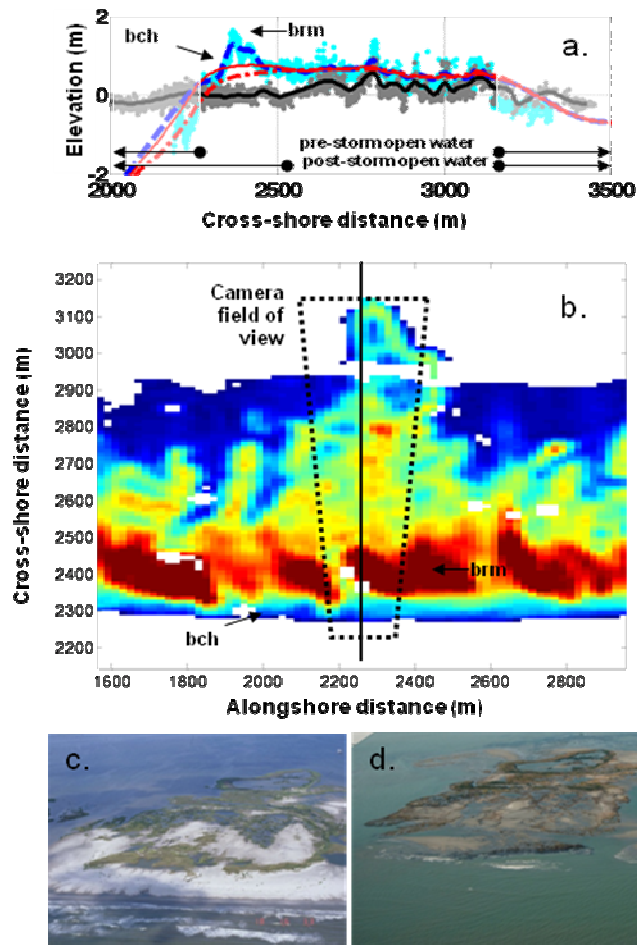
Figure 5.6: Observed (a) pre-storm (blue line; dots show raw data) and post-torm (black) lidar and post-storm model elevation cross-sections (red; solid line=one storm simulation; dash-dot=3 storm simulations). Open water areas have been masked with light transparency. The map view (b) shows the cross-section location and the viewpoint corresponding to pre- and post-storm photographs (c,d).
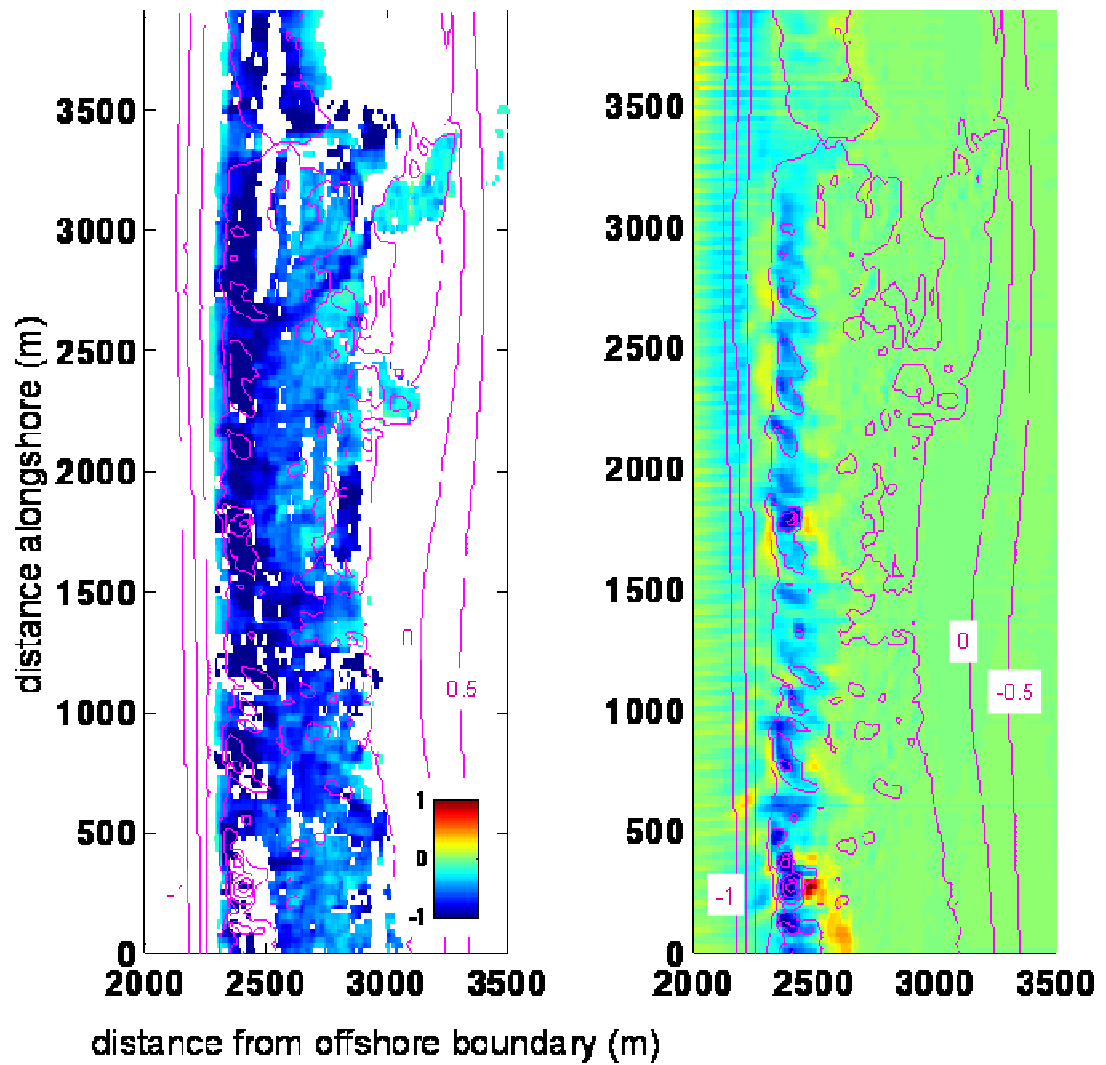
Figure 5.7: Colormaps showing observed (left) and simulated (right) island elevation changes (meters). Deposition is shown as warm colors and erosion as cold colors. Contours show initial island elevations (interval 0.5 m).

maximum erosion occurred along the berm crests, and deposition occurred both in front of and behind the original berm locations. The largest amount of deposition corresponded to infilling of local depressions. There is no evidence of an overwash fan.

5.6   Discussion

There are a number of inherent errors with hindcast simulations using numerical models. In modeling with XBeach, we are interested in understanding the possible sources of error to explain the under prediction of simulation results compared to the erosion inferred from the lidar data. For instance, the boundary forcing, with simulated hydrodynamic conditions, may have produced conditions that were not an accurate representation of Katrina's forcing. However, this is not a likely error source since (1) the boundary forcing conditions have been extensively evaluated and errors in surge and wave height are relatively small compared to the maximum values and (2) the evidence for inundation regardless of these errors is overwhelming.   A sensitivity study was completed evaluating how small changes in the forcing conditions would affect the final morphology. It was found that small changes in the forcing conditions resulted in only small changes in the model skill, highlighting that small errors in the hydraulic boundary conditions did not result in excessive errors in the simulated bed elevation.

Alternatively, the physical processes that were resolved with the model equations may not have captured all of the dominant processes. For instance, the presence of vegetation is ignored in our implementation. It is possible that the important processes were not adequately resolved by the spatial or temporal resolution of the model. The temporal resolution is of interest because of the implementation of the separation of morphological and hydrodynamic time scales. We examine the influence of variations in the

81

morfac parameter, *m*. Furthermore, the initial topography (sampled in 2002) cannot be accurate as an appropriate initial condition for a storm occurring three years later. We investigate the impact of changing the spatial grid resolution of the initial topography, thereby "smearing" the topographic details in order to determine if grid resolution errors are relevant. Finally, we examine the impact of including additional storms on the simulation accuracy.

5.7   Spatial Resolution Sensitivity Study

The spatial resolution used in the analysis presented so far was 10 m cross-shore and 20 m alongshore and was chosen to minimize errors that might result from under-resolving short scale topographic features such as the berm and other features shown in the island cross-section (Figure 5.6). The overall domain size included 66,300 computational nodes. Because the choice of resolution might affect the results, two additional grid resolution scenarios were tested. A grid with a finer resolution than the original grid was chosen with a domain that had 188,370 computational nodes, an alongshore grid spacing of 10 m and a cross-shore resolution of 5 m in the area of interest. A coarser resolution was selected that had an alongshore grid spacing of 40 m, and a cross-shore spacing varying from 50 m offshore to 30 m in the areas where significant topographic changes were observed and required 11,368 computational nodes. The rms difference between the finer resolution (taken to be more faithful to the real topography) and the original grid was 0.06 m, which is less than the expected lidar system errors. The difference between the coarse and fine resolution was also about 0.06 m. This indicates that all three spatial resolutions were generally adequate for resolving the initial topography.

The finer and coarser resolutions were used to simulate the response to Hurricane Katrina. The variations in resolution altered the level of detail of the simulated morphological evolution (Figure 5.8). The coarse resolution simulation lacks fine scale details of the smaller cuts and berm features while the output from the fine resolution simulation captures small-scale morphological features. However, given that there were substantial uncertainties in the model inputs, it is not clear that the higher resolution is justified. In order to quantify these results, the relative error in the island elevation predictions, *RE*, is calculated as

$$RE = \frac{(XBeach_{Final} - lidar_{Final})}{(|lidar_{Final} - lidar_{Inital}| + \sigma_{lidar\,Error})} , \quad (5)$$

where the relative error is the difference between the XBeach final data, $XBeach_{Final}$ and lidar post-storm data, $lidar_{Final}$, compared to the magnitude of change in elevation between lidar post-storm, and lidar pre-storm $lidar_{Inital}$, plus an additional error term. The additional error term, $\sigma_{lidar\,Error}$, is related to GPS error associated with lidar data (~0.2 m), and temporal errors (~0.25 - 1.0 m). Assuming the temporal error is 0.4 m, $\sigma_{lidar\,Error}$ is found to be 0.45 m when calculated with

$$\sigma_{lidar\,Error} = \sqrt{(GPS\,error)^2 + (Temporal\,error)^2} , \quad (6)$$

The *RE* was calculated for the three resolution cases (Table 5.1).   Relative errors greater than 1 signify serious failure of the model, as the magnitude of the errors would exceed the magnitude of changes that we intended to predict. The three resolutions tested in this study all showed *RE* less than 1, indicating the model did not fail in any of the

three cases. However, the *RE* was typically greater than 50%. The errors were also similar, varying 1% at maximum, for each of the resolutions, indicating that the highest resolution implementation, which was the most computationally expensive, did not provide significant benefit over the medium and coarse resolutions. It is clear from this analysis that the coarse resolution would actually suffice for simulating this scenario in spite of the apparent loss of detail. The

apparent lack of preference for high resolution may be due to the fact that the post-storm topography was devoid of major short-scale features. Compared, for instance, to remnant high dunes in the McCall (in press) study of Santa Rosa Island, the Chandeleurs are well-resolved with the coarse resolution.

5.8   Temporal Resolution Sensitivity Study

The sensitivity to the morfac parameter, *m*, was also tested. As with the spatial resolution, we used both finer (value of 1) and coarser (value of 20) parameterizations compared to the original choice of 10. Again, the relative errors associated with each simulation were calculated (Table 5.2), and indicated there was little to no difference, 2% at most, in errors under different morfacs. Again, it is clear that coarser temporal resolution of the morphologic response would have been justified and that little would be gained from finer resolution. This may be related to the magnitude of the initial condition errors, which, perhaps, dominate other error terms and reduce sensitivity to choices in factors such as morfac parameter or grid resolution.

Relative Error Bins for Resolution			
Relative Error	Fine	Medium	Coarse
R.E. >100%	0.000	0.000	0.000
100% >= R.E. > 75%	0.106	0.098	0.097
75% >= R.E. > 50%	0.718	0.719	0.728
50% >= R.E. > 25%	0.110	0.118	0.111
25% > = R.E. > 10%	0.016	0.014	0.015
10% > R.E.	0.011	0.011	0.011

Table 5.1:   Relative error bins for three grid resolutions.

Relative Error Bins for Morfac			
Relative Error	Morfac 1	Morfac 10	Morfac 20
R.E. >100%	0.000	0.000	0.000
100% >= R.E. > 75%	0.098	0.098	0.106
75% >= R.E. > 50%	0.725	0.719	0.705
50% >= R.E. > 25%	0.109	0.118	0.126
25% > = R.E. > 10%	0.017	0.014	0.015
10% > R.E.	0.012	0.011	0.010

**Table 5.2:   Relative error bins for three morfacs.**
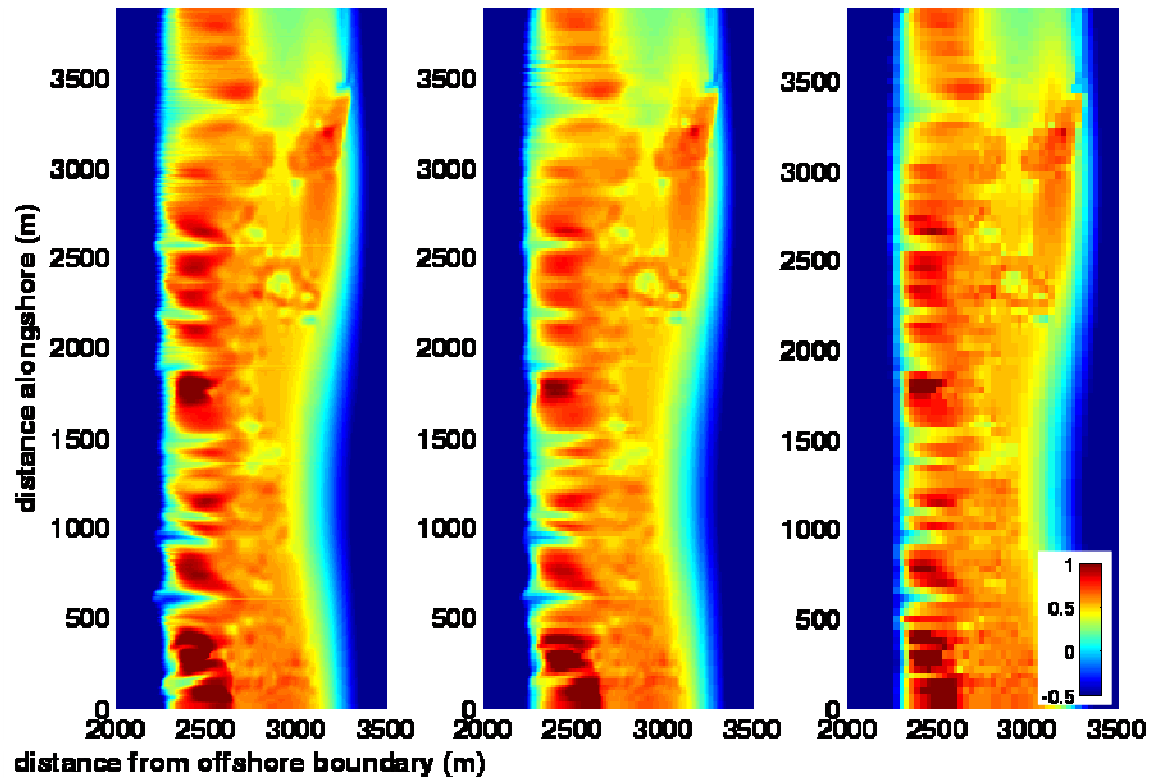
Figure 5.8: Simulation results using fine (left), medium (middle), and coarse (right) grid resolutions. Color scale is elevation in meters.

5.9 Multiple Runs

To explore the impact of using out-of-date initial topography, it is of interest to see how the Chandeleur Islands evolve after several severe hurricanes impact the island. Ideally, we would simulate all of the actual storms occurring since the 2002 lidar data were collected. However, this would be computationally prohibitive and is beyond the scope of this study. Instead, we simulated the effect of multiple storms by running several Katrina-type events over the island to determine how XBeach predicts this morphologic evolution over multiple events. Since there were several storms between the survey conducted in 2002 that provided initial bathymetry data and landfall of Hurricane Katrina in 2005, it is possible that simulation of intervening storms could reduce the mismatch between the observed and simulated post-Katrina topography. Instead of simulating the intervening storms (Lili, Isidore, Ivan, and Cindy), we use sequential forcing based on Katrina as a proxy.

Three additional storm simulations were conducted using the original choices of grid resolution and morfac, m. The topography after the first through fourth simulations is shown in Figure 5.9. Breakup of the islands becomes more pronounced as cuts grow and deepen. After each consecutive run of Hurricane Katrina storm conditions, additional losses of subaerial island area and generally lower elevations result. On average, 2% of the initial (2002) island area was lost after each run, and a total of 8.4% is lost between run one and four. By the fourth run of Katrina, morphology starts to resemble the post-Katrina structure of the islands, with heavy segmentation. The statistical analysis of the results was based on two classes of points that were divided according to whether land was converted to open water or not. In this case, land was defined as topography with elevation above -0.5 m (Figure 5.5, right-hand panel). (A discussion of datum choice is given in Section

88

5.4) Locations where observations showed that the initial topography was not converted to open water (i.e., land-to-land points) were not correlated to the simulated changes given one Katrina run, as mentioned before (Figure 5.5). Table 5.3 indicates the change in the simulation errors as a function of the number of simulated storms. Land-to-land points after multiple runs showed slight reductions in the mean error as the subsequent storms increased the total amount of erosion. Other statistics that were computed included the total root mean square error (which include both mean and random errors), and the skill (squared correlation of the regression). For the land-to-land points, the skill and the total error are not affected. XBeach has no skill predicting the variation in erosion of these points, most likely due to the points being marshland but modeled as sand in XBeach (see Section 5.10).

Points that were observed to develop from land to open water (land-to-water) showed a strong correlation between simulated and observed changes over a single Katrina run. Specifically, these points yield a regression gain of about one, and a regression skill of 0.4 (Table 5.3). With additional runs of Katrina, the mean error was reduced as elevations generally become lower. The total error (includes both mean and random components) decreases until three simulations have been performed. The gain and skill degrade under further simulations. This reflects the increased scatter in the correlations shown in Figure 5.5. The total error is nearly constant after three simulations, suggesting that a balance is reached between improved simulation accuracy as island height is reduced and reduced accuracy due to poorly-predicted details as the island is dissected. This is further suggested by Figure 5.9, where the simulated island development begins to resemble better the appearance of the islands post-Katrina. However, the exact location of cuts and remnant berms are poorly predicted, adding to increased total errors.

	Mean error (m) land (water)	RMS error (m) land (water)	Skill (m) land (water)
Persistence	0.38 (0.48)	0.40 (0.55)	--
1 Katrina	0.37 (0.41)	0.39 (0.46)	0.01 (0.41)
2 Katrinas	0.36 (0.36)	0.39 (0.43)	0.00 (0.35)
3 Katrinas	0.35 (0.30)	0.39 (0.40)	0.00 (0.34)
4 Katrinas	0.35 (0.24)	0.39 (0.41)	0.00 (0.31)

Table 5.3:   Error and skill parameter for multiple Katrina Simulations

5.10 Cape Henlopen

After determining that XBeach had the capability to simulate tropical storms on a barrier island with robust skill and accurate identification of erosion patterns, the model was selected to use at the Cape Henlopen site for an initial analysis, simulating Tropical Storm Bonnie.

Tropical Storm Bonnie originated off of the coast of Africa, developing into a major hurricane as it moved through the Atlantic Ocean. It made landfall in North Carolina early 27 Aug 1998 as a strong Category 2 storm, with wind gusts up to 167 km/hr. Once making landfall it lost hurricane status, affecting the Delaware coastline with large waves and coastal erosion as an offshore tropical storm. The storm regained hurricane status 28

Aug 1998, while in the Atlantic ocean until moving into cooler ocean waters off the coast of

Newfoundland 30 Aug 1998 (Avila, 1998) (Figure 5. 10) where it finally died.
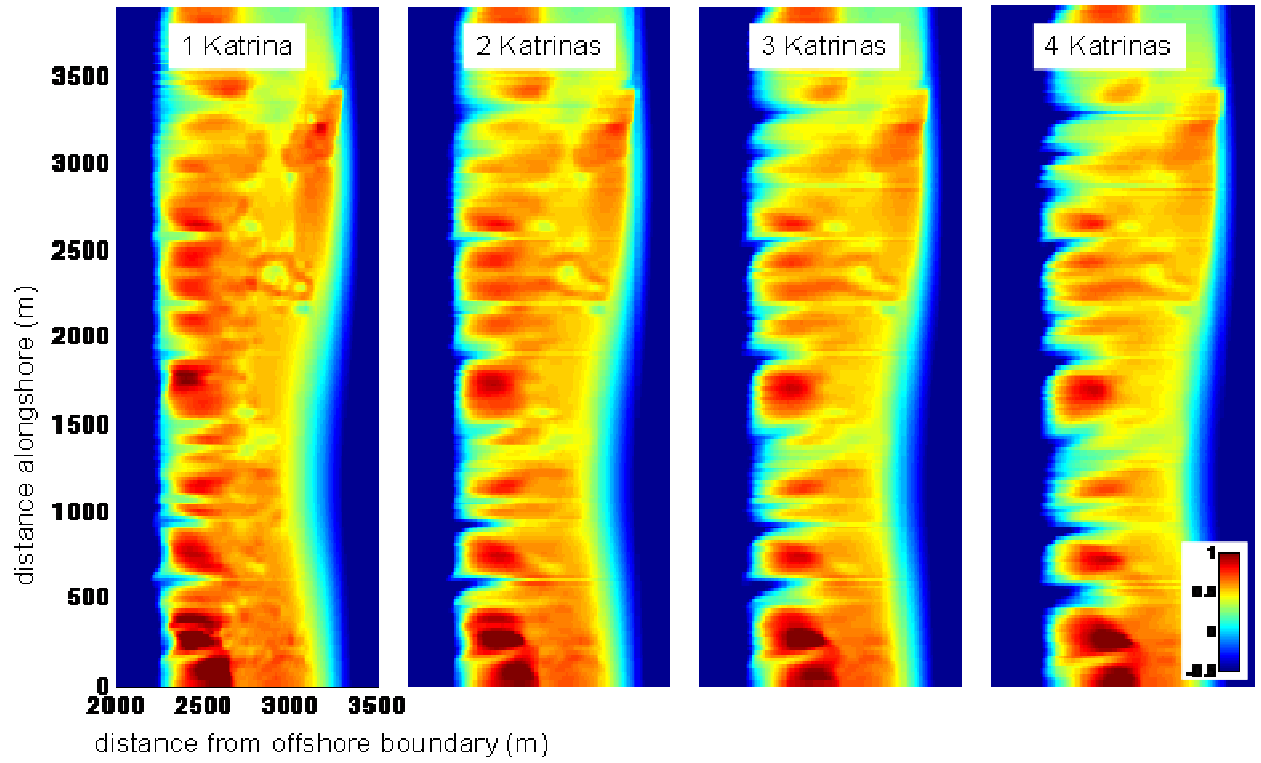
Figure 5.9: Simulated island evolution after 1-4 consecutive storms. Colorscale is elevation in meters.

Although the storm did not make landfall in Delaware, its affects were strongly felt throughout the Delaware coastal region. In Rehoboth Beach, Delaware, slightly south of our AOI, a person drown as a result of rip currents caused by Tropical Storm Bonnie (Avila, 1998). Higher than normal waves and strong currents plagued the area during the storm.

For the XBeach simulation of Tropical Storm Bonnie, wave conditions were taken from a set of public off shore wave data produced by the USACE's WIS model. WIS data provides hindcast, nearshore conditions given as frequency-directional spectrums for the selected location and time period. Wave conditions were given in three hour time increments during the duration of the storm, providing details on the significant wave height, direction and period. The wave data were used to produce a parameterized Jonswap spectrum describing the short wave information. The Jonswap spectrum forced the model simulation, from the offshore boundary. The model was forced from 27 Aug 1998 21:00 to 29 Aug 1998 12:00. The peak significant wave height was 4.2 m with a mean wave period of 9.9 s (Figure 5.11). During the storm, the wave direction varied from 141 nautical degrees as the storm approached to 176 nautical degrees as the storm left the Delaware coastline.

Available bathymetry data for the site included Delaware Geological Survey lidar data from 2005 for the subaerial and a conglomeration of NOAA offshore bathymetry data from the late 1800s to present, available at the National Geophysical Data Center's website. The data sets were combined and interpolated using an inverse weighting function to grid the study area. A radial search distance of 60 m was used for the nearshore and subaerial locations, and a radial search distance of 1000 m (due
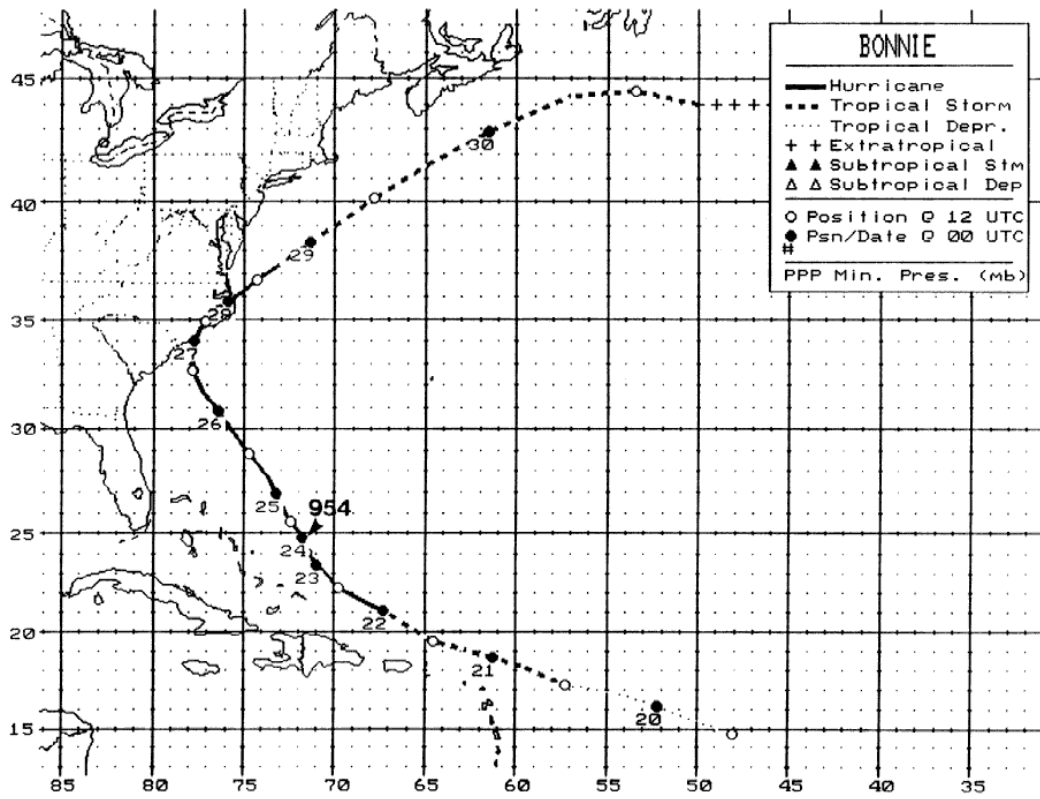
**Figure 5.10:** Track of Hurricane Bonnie August 19-30, 1998. (Avila, 1998).
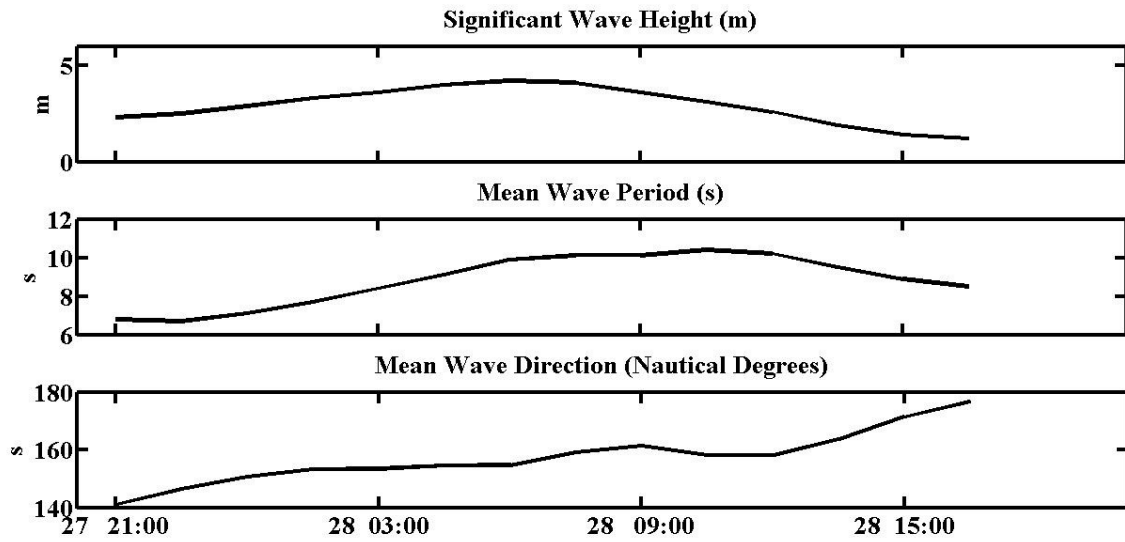
Figure 5.11: The wave conditions used to force the model. The significant wave height (m), mean wave period (s) and mean wave direction (nautical degrees) were supplied from the USACE WIS data set. The x-axis shows the time the model is forced, for 27 Aug 1998 21:00 to 29 Aug 1998 12:00.

to scarce data) was used in the offshore region, resulting in a fusion of data creating the input bathymetry for the test (Figure 5.12).

The study site is a grid (size: [90 637]) with a longshore resolution of 90 m, and a spatially varying cross-shore resolution of 5 m in the nearshore to 50 m in the offshore region. The domain is a 1.8 x 15 km rectilinear grid. Such a large cross-shore grid domain is not ideal, but without available wave data modeled to the desired offshore wave boundary, the offshore boundary must be the WIS data buoy.

The initial results, forcing the available bathymetry with the WIS wave data, produced imperfect results (Figure 5.13). XBeach suggested that the shoals were the only location of major erosion, and deposition (Figure 5.13), leaving the shoreline relatively untouched. The shoals have now emerged above water, and are starting to form barrier islands. This is beyond the realm of possibility in this area, at this timescale. The massive errors are probably due to initial errors from sparse available bathymetry to a grid and the location of available wave data. The obtainable bathymetry in the offshore region had an undesirable spacing (on the order of hundreds of meters), much too coarse for accurate results. The simulation does not include the currents from the strong tidal jet leaving the Delaware Bay that influences this area with each ebb tide. The cross-shore size of the grid (15 km) is also a probable the cause of the unreliable model results. This initial exploration has provided us with guidelines (less coarse data set, model wave data closer to the AOI) for data collection in order to complete a successful investigation of the Delaware coastline using XBeach.
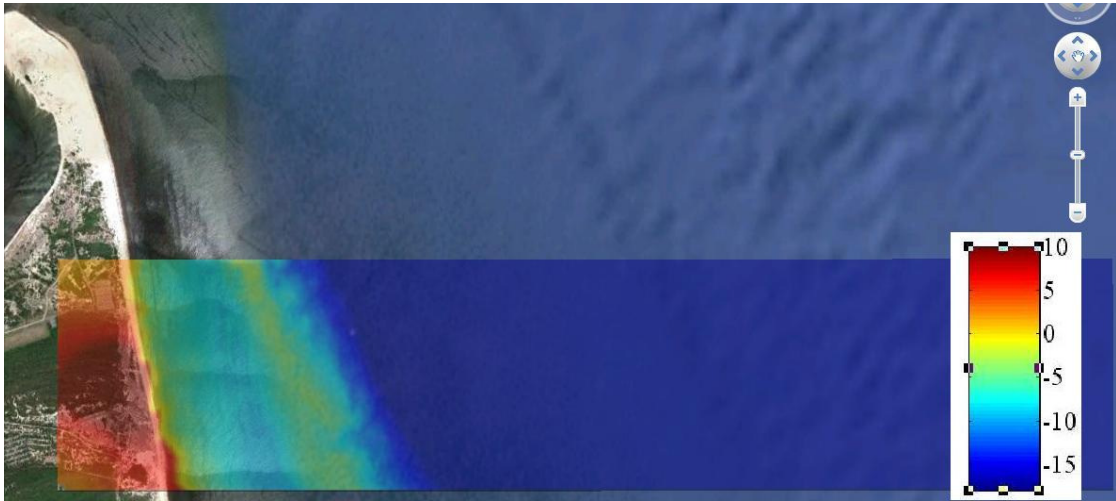
Figure 5.12:   The Cape Henlopen XBeach study site overlaid on Google Earth. Subaerial topography is from Delaware Geological Survey lidar surveys (2005), and bathymetry is a conglomeration of data from the late 1800's to present available at NOAA's National Geophysical Data Center website. The colorbar inset provides elevation (m), over the 1.8 x 15 km site.
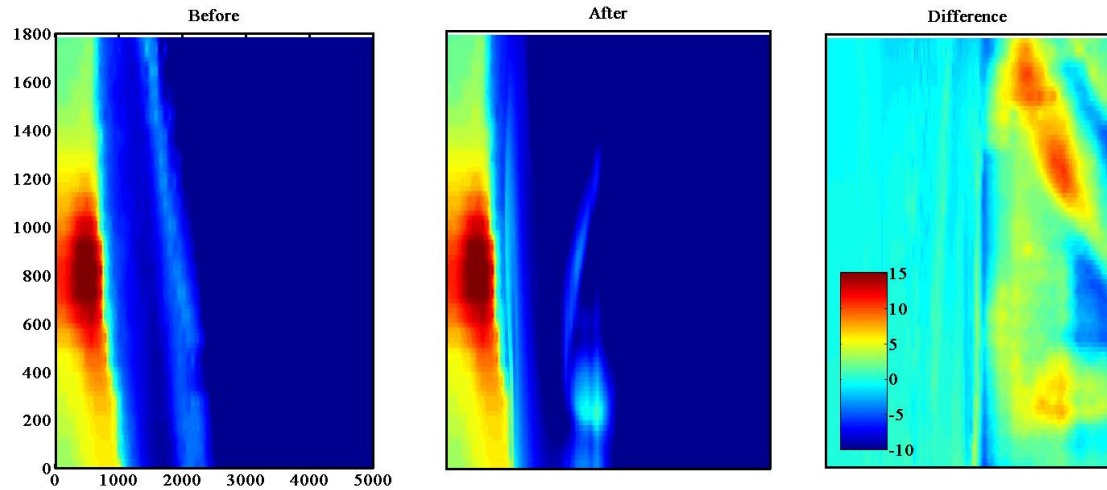
Figure 5. 13: The left figure shows the study site prior to simulation (distances and colorbar are in meters). The center figure shows the bed level post-simulation, where the shoal has reshaped. The right shows the change in the bed level (final - initial), and shows the change in the shoal. The change is on an excessive scale, and is unmistakably false, considering the shoals have now formed islands.

Chapter 6

FUTURE WORK

The Delaware coastline provides an interesting backdrop for coastal morphological studies. The extreme growth at the Cape, and deficiency of recent data sets exploring the changing landscape and hydrodynamic conditions governing these changes, put it at the forefront of necessary areas to study in the region. This initial exploration of the techniques possible to use to evaluate these processes has provided an outline of future routes and methods that will allow for more definitive conclusions on what is occurring in this region. The video-imaging system, once re-instated, will be successful in remotely providing an automatic and accurate dataset of shoreline position over time, while also providing insight into the varying breaker zone intensity that appears on the northern section of the Cape.

Continuous surveys of the beach will allow further conclusions to drawn on the erosional and deposition patterns found in the area, from small scale features such as discussed in Section 3.4, and large scale growth and change of beach width as discussed in Section 3.2. Additional surveys, spanning several seasons of different hydrodynamic conditions provide answers about the rate of evolution at the Cape. Coupled with further sensor deployments, as discussed in Chapter 4, the evolutionary patterns can be paired with known currents providing further verification of the prevailing patterns.

Survey datasets are vital to provide accurate and dense initial input into XBeach. With extensive surveying completed before and after storm events in the region,

comparison and additional model verification can be complied, allowing for the

development of XBeach in to a predictive tool for the Delaware coastline, as it has been for

the region of the Chandeleur Islands.

REFERENCES

Aarninkhof, S. and Holman, R.A., 1999. Monitoring the nearshore with video. Backscatter, 10 (2), pp. 8-11.

Avila, L., 1998. Preliminary report Hurricane Bonnie 19-30 August 1998, National Hurricane Center.

Brock, J.C., Wright, C.W., Sallenger, A.H., Krabill, W.B., and Swift, R.N., 2002. Basis and methods of NASA Airborne Topographic Mapper lidar surveys for coastal studies. Journal of Coastal Research, 18 (1), pp. 1-13.

Cañizares, R., and Irish, J. L., 2008. Simulation of storm-induced barrier-island morphodynamics and flooding, Coastal Engineering, 55. pp. 1089-1101

Cowell, P.J., Roy, P.S., and Jones, R.A., 1995. Simulation of large-scale coastal change using a morphological-behaviour model, Marine Geology, 126, pp. 45-61.

Chrysalis Consulting, Inc., 2007. The economic effects of a five year nourishment program for the ocean beach of Delaware, Updated. Submitted to Anthony P. Pratt, DNREC.

Demarest, J.M., 1978, The shoaling of Breakwater Harbor, Cape Henlopen Area, Delaware Bay, 1842 to 1971. Delaware Sea Grant Technical Report, College of Marine Studies, University of Delaware.

Demarest, J.M., and Kraft, J.C., 1979. Projection of sedimentation patterns in Breakwater Harbor, Delaware. Shore and Beach, April, pp. 17-24.

Hayden, J.T., 2009. Indian River Inlet bridge and bathymetry scour monitoring system, Master's Thesis, University of Delaware.

Holland, K.T., Holman, R.A., Lippmann, T. C., Stanley, J. and Plant, N., 1997. Practical use of video imagery in nearshore oceanographic field studies. IEEE Journal of Oceanic Engineering, 13 (1), pp. 81-92.

Holman, R.A., Stanley, J. (2007).The history and technical capabilities of Argus. Coastal Engineering, 54, 477-491.

Hoyt, W.H., 1982. Processes of sedimentation and geological history of the Cape Henlopen/Break Water Harbor Area, Delaware. Ph.D. dissertation, University of Delaware.

Interagency Performance Evaluation Task Force, 2007. Performance evaluation of the New Orleans and southeast Louisiana Hurricane Protection System, final report of the Interagency Performance Evaluation Task Force, Vol. IV—The storm. US Army Corps of Engineers, Washington, DC

Jiménez, A.H. Sallenger and L. Fauver, Sediment transport and barrier island changes during massive overwash events, 2006, *ICCE,* 2006, San Diego.

Kahn, J.H., 1986. Geomorphic recovery of the Chandeleur Islands, Louisiana, after a major hurricane. Journal of Coastal Research, 2 (3), pp. 337-344.

Knabb, R., Rhome, J., and Brown, D. 2005. Tropical Cyclone Report: Hurricane Katrina, National Hurricane Center, Miami, FL.

Kraft, J.C., and Caulk, R.L., 1972. The evolution of Lewes Harbor. Transactions of the Delaware Academy of Sciences 1970 and 1971. pp. 79-125.

Lesser, G., Roelvink, J.A., van Kester T.A., and Stelling, G.S, 2004. Development and validation of a three-dimensional morphological model, Coastal Engineering, 51. pp. 883–915.

Lindemer, C.A., 2008. Coastal Imaging at Cape May, New Jersey. Senior Thesis, University of Delaware.

Luettich, R.A., Jr., Westerink, J.J. and Scheffner, N.W., 1992. ADCIRC: an advanced three-dimensional circulation model for shelves, coasts and estuaries, report 1: theory and methodology of ADCIRC-2DDI and ADCIRC-3DL, Technical Report DRP-92-6. Department of the Army, US Army Corps of Engineers, Waterways Experiment Station, Vicksburg, MS, pp. 1-137.

MacMahan, J. H., 2001. Hydrographic surveying from personal water-craft. Journal of Surveying Engineering. 127 (1), pp 12-24.

Maurmeyer, E.M., 1974. Analysis of short- and long-term elements of coastal change in a simple spit system: Cape Henlopen, Delaware. Master's Thesis, University of Delaware.

McCall, R.T., Van Thiel de Vries, Plant, N.G., Van Dongeren, A.R., Roelvink, J.A., Thompson, D.M., Thompson, D.M., in press. Two-dimensional time dependent Hurricane overwash and erosional modeling at Santa Rosa Island, submitted to Coastal Engineering.

Pearre N.S., and Puleo, J.A., 2009. Quantifying seasonal shoreline variability at Rehoboth Beach, Delaware, using automated imaging techniques. Journal of Coastal Research: 25 (4), pp. 900-914.

Plant, N.G., Edwards, K.L., Kaihatu, J.M., Veeramony, J., Hsu, L., and Holland, K.T., 2009. The effect of bathymetric filtering on a nearshore process model, Coastal Engineering, 56, pp.484–493.

Plant, N.G., Holland, K.T. and Puleo, J.A., 2002. Analysis of the scale of errors in nearshore bathymetric data. Marine Geology, 191, pp. 71-86.

Pratt, J. C., 2007. Cape Henlopen Spit complex and recent evaluation of Breakwater Harbor, Lewes, Delaware. Master's Thesis. University of Delaware.

Puleo, J.A., 2009. Quantifying short-term morphologic evolution and alongshore sediment transport rates at Cape Henlopen, DE using remote sensing and rapid-response GPS-equipped vehicles. Proposal submitted to Sea Grant.

Puleo, J.A., 2010. Estimation alongshore sediment transport and the nodal point location on the Delaware-Maryland Coast. Journal of Waterway, Port, Coastal and Ocean Engineering, 136(3).

Ramsey, W.R, and Wang, L.T., 2001. Historical coastline changes of Cape Henlopen, Delaware. Delaware Geological Survey Special Publication, 26.

Roelvink, J.A., Reniers, A., Van Dogeren A., Van Thiel de Vries, J., McCall, R., and Lescinski. J., 2009. Modeling storm impacts on beaches, dunes and barrier islands. Coastal Engineering, 56, pp. 1133-1152.

Rosati, J. D., Stone, G.W., Dean, R.G., and Kraus, N.C., 2006, Restoration of barrier islands overlying poorly-consolidated sediments, south-central Louisiana: Gulf Coast Association of Geological Societies Transactions, 56, pp. 727-740.

Sallenger, A.H., 2000. Storm impact scale for barrier islands. Journal of Coastal Research, 16(3), pp. 890-895.

Smith, J.M., Sherlock, A.R., and Resio, D.T., 2001. STWAVE: Steady-State Spectral Wave Model User's Manual for STWAVE, Version 3.0. Coastal and Hydraulics Laboratory ,U.S. Army Engineer Research and Development Center, Vicksburg, MS pp. 1-81.

Stockdon, H., Sallenger, A., Holman, R., and Howd, P., 2006. A simple model for the spatially-variable coastal response to hurricanes, Marine Geology 238, pp. 1-20.

Stolper, D., List, J.H., and Thieler, E.R., 2005. Simulating the evolution of coastal morphology and stratigraphy with a new morphological-behavior model (GEOMBEST). Marine Geology, 218, pp. 17-36.

Turner, I.L., Aarninkhof, S., and Holman R.A., 2006. Coastal imaging application and research in Australia. IEEE Journal of Coastal Research, 22 (1), pp. 37-48.

Twichell, D., Pendleton, E., Baldwin, W., and Flocks, J. 2009. Subsurface control on seafloor erosional processes offshore of the Chandeleur Islands, Louisiana. Geo-Marine Letters, 29, pp. 349-358.

United States Army Corps of Engineers, 1994. Indian River Inlet: An evaluation by the committee on tidal hydrodynamics.

van Thiel de Vries, J.S.M., van Gent, M.R.A., Walstra, D.J.R., and Reniers, A.J.H.M., 2008. Analysis of dune erosion in large scale flume experiments. Coastal Engineering, 55 (12), pp. 1028-1040.